WATER RESOURCES RESEARCH, VOL. 37, NO. 8, PAGES 2019–2035, AUGUST 2001

On the continuum-scale modeling of gravity-driven fingers in unsaturated porous media: The inadequacy of the Richards equation with standard monotonic constitutive relations and hysteretic equations of state

Mehdi Eliassi and Robert J. Glass

Flow Visualization and Processes Laboratory, Sandia National Laboratories, Albuquerque, New Mexico

Abstract. We consider the ability of the continuum-scale Richards equation (RE) with standard monotonic constitutive relations and hysteretic equations of state to model gravity-driven fingers in unsaturated porous media and, in particular, the underlying nonmonotonicity observed along the vertical extent of fingers. As published in a number of recent papers, finger-like solutions with nonmonotonic profiles can be simulated numerically using a downwind averaging method. However, we find these fingers to be artifacts, generated by the combined effects of a truncation error induced oscillation or oversaturation at the wetting front, and capillary hysteresis. As the oscillation is removed, either through grid refinement or the use of inherently monotone schemes, the numerically generated fingers disappear, and the solution becomes monotonic. Thus the RE along with standard monotonic hydraulic properties does not contain the critical physics required to model gravity-driven fingers and must be considered inadequate for unsaturated flow in initially dry, highly nonlinear, and hysteretic media where these fingers occur.

1. Introduction

Gravity-driven fingers in unsaturated porous media were noted by a number of early researchers [e.g., *Palmquist and Johnson*, 1960, 1962; *Tabuchi*, 1961; *Peck*, 1965] and formally connected to the instability of a downward advancing wetting front (WF) by *Hill and Parlange* [1972]. Subsequent experimental observations in initially dry, water-wettable, homogenous sands at low supply rates and where the air phase could escape freely, revealed that, as a finger grows downward, its tip oversaturates and then drains a distance behind [e.g., *Glass et al*., 1989b; *Selker et al*., 1992]. In a hysteretic medium such a nonmonotonic response induces heterogeneity in hydraulic properties and produces a finger core and fringe region structure that persists in time and over subsequent drainage and infiltration cycles. In fact, as noted by *Glass and Nicholl* [1996], from the time of the initial finger formation onward, system behavior is controlled not by WF instability but by the heterogeneous field; subsequent infiltration cycles simply follow the hysteresis-induced template of the initial unstable event. Thus the oversaturation and subsequent nonmonotonic behavior demonstrated by gravity-driven fingers is an essential characteristic of the phenomenon and in combination with hysteresis controls subsequent system evolution. While gravity-driven fingering in unsaturated media is actually stabilized by viscous forces, it is often considered to be a subset of viscous fingering after the early theoretical and experimental works of *Saffman and Taylor* [1958] and *Chouke et al*. [1959]. However, the nonmonotonic signature of gravity-driven fingers fundamentally separates the critical physics of these two classes of fingering.

Recently, *Nieber* [1996] simulated gravity-driven fingering in initially dry, highly nonlinear, and hysteretic porous media using continuum representations of the physics as embodied in Richards equation (RE) along with standard constitutive relations and hysteretic equations of state [*Mualem*, 1974, 1976; *van Genuchten*, 1980], hereafter referred to as "standard monotonic properties." *Nieber* [1996] found, however, that the hydraulic conductivity values across two nodes (i.e., the internodal averages) must be calculated with weighting toward the downwind node, otherwise fingers do not form. By varying the weighting parameter within the downwind averaging method at a given spatial grid spacing, *Nieber* [1996] was able to calibrate his results to reasonably match the finger widths found experimentally by *Glass et al*. [1989a, 1989c]. Additionally, *Nieber*'s [1996] simulations reflect the essential nonmonotonicity that is characteristic of gravity-driven fingers. These initial simulations have subsequently been extended in a series of papers that study gravity unstable flow and solute transport in water-repellent sandy soils [*Ritsema et al*., 1998a, 1998b; *Nguyen et al*., 1999a, 1999b; *Nieber et al*., 2000]. Additionally, in the work of *Ritsema et al*. [1998a] the full two-phase flow form of the governing equations (i.e., equations for both air-water) were implemented, again with downwind averaging for the water phase.

The apparent success and growing use of *Nieber*'s [1996] approach suggests that indeed, the RE, or its two-phase flow equivalents for the air-water system, are the correct governing equations for unsaturated flow in the range of parameter space where fingers occur. However, the RE and its two-phase equivalents are continuum-scale parabolic partial differential equations (PDEs), which for constant flux boundary conditions and standard monotonic properties should admit only monotonic solutions that are bounded by the initial and boundary conditions [e.g., *Rubin and Steinhardt*, 1963; *Rubin et al*., 1964; *Youngs*, 1995]. Thus, considering the fundamental behavior of

Paper number 2000WR900403.

such parabolic PDEs as diffusive, we pose the question: Why does *Nieber*'s [1996] approach simulate fingers and their inherent nonmonotonic signature when for constant flux infiltration the RE should yield a monotonic response?

To answer this question, we formulate a numerical solution of the RE with standard monotonic properties that implements a variety of averaging methods including downwinding. Illustrative simulations demonstrate that, while downwind averaging is capable of yielding "finger-like" solutions, other averaging methods yield diffusive (i.e., "nonfingered") responses. To understand why downwind averaging yields fingers, we consider the leading truncation error (LTE) terms associated with the numerical discretizations and derive the modified governing equation that is actually being solved by each averaging method. Analysis of the LTE terms' behavior across the WF shows that fingers simulated with downwinding are numerical artifacts, entirely due to a truncation error induced oscillation or oversaturation at the WF combined with capillary hysteresis. These results support our thesis that the RE with standard monotonic properties does not incorporate the critical physics required to model gravity-driven fingers and must be considered inadequate in the range of parameter space where such fingers occur.

2. "Finger-Like" Solutions From Richards Equation

Nieber [1996] adopted a Galerkin Finite Element Method (FEM) with bilinear (four-node quadrilateral) elements to discretize the spatial terms in the two-dimensional (2-D) form of the RE and used a fully implicit first-order backward Euler scheme [e.g., *Celia et al*., 1990] to discretize the temporal term. He also used the standard monotonic properties of *van Genuchten* [1980] and *Mualem* [1976] with *Mualem*'s [1974] independent domain hysteresis model. *Nieber* [1996] linearized the resulting nonlinear system of algebraic equations based on the modified-Picard iteration (MPI) method of *Celia et al*. [1990], and during each nonlinear iteration step the system of linear equations was solved using a preconditioned conjugate gradient method. Most of these features are relatively standard. However, *Nieber* [1996] also implemented several nonstandard features such as setting the hydraulic conductivity to zero when the water content was below the residual moisture content of the main drainage curve (MDC); considering an air-dry or primary wetting curve (PWC) that is artificially depressed (i.e., the PWC has a near-zero water-entry pressure); forcing a jump from the PWC to the MDC when saturation on the PWC is ~0.99; and most importantly, using downwind averaging to evaluate the internodal conductivity values at the WF. As stated by *Nieber* [1996] and confirmed by us, the critical finger forming nonstandard feature is the downwind averaging of internodal conductivity.

In the following sections, we present our numerical solution of the RE with standard monotonic properties and consider its behavior in a region of parameter space where fingers form experimentally. In section 2.1 we summarize our initial boundary value problem (IBVP) based on a 2-D dimensionless form of the RE. In section 2.2 we describe our numerical solution procedure using several first-, second-, and third-order accurate internodal averaging methods in detail. In section 2.3 we present a series of illustrative 2-D numerical results that demonstrate both the success and failure of the various averaging techniques to yield finger-like solutions. These results indicate that the simulated critical characteristics of finger behavior do not arise from the physics embodied in the RE, but from artifacts introduced by the numerical technique.

2.1. RE, Standard Monotonic Properties, and Initial-Boundary Conditions

In the following development, the dimension of a variable or system parameter is given in brackets when first defined. For unsaturated flow under isothermal conditions and assuming negligible resistance to water flow by the air phase, the traditional two-phase flow equations reduce to the well known single-phase form of the RE. We write the single-phase, time-dependent, pressure-based form of the RE in 2-D Cartesian coordinates as

$$C(\psi)\frac{\partial\psi}{\partial t} - \left\{\frac{\partial}{\partial x}\left[K(\psi)\frac{\partial\psi}{\partial x}\right] + \frac{\partial}{\partial z}\left[K(\psi)\frac{\partial\psi}{\partial z}\right]\right\} = \frac{\partial}{\partial z}K(\psi), \tag{1}$$

where $C(\psi)[L^{-1}]$ is the slope of the moisture-retention curve commonly referred to as the water capacity function, $\psi[L]$ is the pressure head, $t[T]$ is the time, $x[L]$ and $z[L]$ are the horizontal and vertical directions, respectively, and $K(\psi)[LT^{-1}]$ is the hydraulic conductivity function. We define the functional forms of the equation of state (i.e., the moisture-retention relation) and the constitutive relation (i.e., the hydraulic conductivity function) using the standard monotonic models of *van Genuchten* [1980] and *Mualem* [1976], respectively, as

$$\Theta_H(\psi) \equiv [(\theta_H(\psi) - \theta_r)/(\theta_s - \theta_r)] = [1 + (\alpha_c|\psi|)^n]^{-m} \tag{2a}$$

$$K(\Theta) = K_s\sqrt{\Theta_H(\psi)}\,[1 - (1 - \Theta_H(\psi)^{1/m})^m]^2, \tag{2b}$$

where $\Theta_H(\psi)$ and $\theta_H(\psi)[L^3L^{-3}]$ are the hysteretic saturation and volumetric moisture content, respectively, as a function of pressure, $\theta_r[L^3L^{-3}]$ and $\theta_s[L^3L^{-3}]$ are the residual and saturated moisture content values, respectively, $\alpha_c[L^{-1}]$ is the inverse capillary length for a given hysteretic moisture-retention branch c (e.g., PWC, MDC, etc.), n defines the media nonlinearity, $m = 1 - (1/n)$, and $K_s[LT^{-1}]$ is the saturated conductivity of the medium. Here we consider only standard monotonic properties and thus take K to be hysteretic with respect to ψ but nonhysteretic with respect to Θ, consistent with the experimental findings of *Topp and Miller* [1966], *Talsma* [1970], and *Vachaud and Thony* [1971]. Finally, we choose to represent hysteresis in $\Theta_H(\psi)$ through the use of *Scott et al*.'s [1983] empirical scaling model. From comparisons to experimental data for sands that support gravity-driven fingering, *Norton* [1995] found this simple empirical model to be of equal accuracy to other more complicated and theoretical approaches [e.g., *Mualem*, 1974, 1984; *Hogarth et al*., 1988].

To simplify our studies, we nondimensionalize (1) and (2) by using the following variables: $\Gamma(\Psi) = C(\psi)/\alpha_{\mathrm{PWC}}$, $\Psi = \psi\alpha_{\mathrm{PWC}}$, $\tau = t(\alpha_{\mathrm{PWC}}K_s)$, $\eta = x\alpha_{\mathrm{PWC}}$, $\xi = z\alpha_{\mathrm{PWC}}$, and $\kappa(\Psi) = K(\psi)/K_s$, where $\alpha_{\mathrm{PWC}}[L^{-1}]$ is the inverse capillary length of the PWC. Here $\Gamma(\Psi)$, Ψ, τ, η, ξ, and $\kappa(\Psi)$ are the dimensionless water capacity function, pressure head, time, horizontal and vertical positions, and hydraulic conductivity function, respectively. Substituting these dimensionless variables into (1) yields

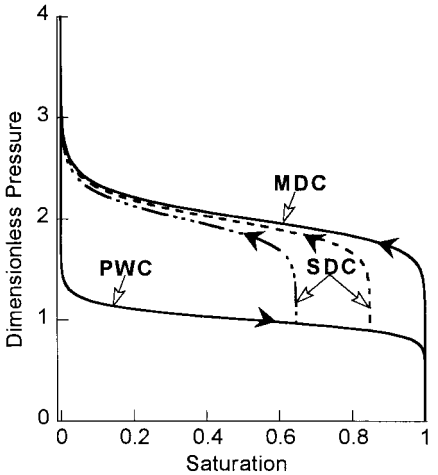

Figure 1. A typical closed-loop hysteresis diagram with PWC and MDC representing the boundary curves along with typical SDCs. In the figure the media nonlinearity parameter for the bounding curves is $n_{\mathrm{PWC}} = n_{\mathrm{MDC}} = 15$, and the maximum hysteresis loop size is $\alpha_H^* = 0.5$. Note that an α_H^* of 1.0 lowers the MDC to overlie the PWC. Such a single curve is used for nonhysteretic cases.

$$\Gamma(\Psi)\,\frac{\partial \Psi}{\partial \tau} - \left\{ \frac{\partial}{\partial \eta}\left[\kappa(\Psi)\,\frac{\partial \Psi}{\partial \eta}\right] + \frac{\partial}{\partial \xi}\left[\kappa(\Psi)\,\frac{\partial \Psi}{\partial \xi}\right]\right\} = \frac{\partial}{\partial \xi}\,\kappa(\Psi) \tag{3}$$

and the dimensionless monotonic properties

$$\Theta_H(\Psi) = [1 + (\alpha^*|\Psi|)^n]^{-m}$$

and (4a)

$$\kappa(\Theta) = \sqrt{\Theta_H(\Psi)}\,[1 - (1 - \Theta_H(\Psi)^{1/m})^m]^2.$$

The dimensionless form of the water capacity function, $\Gamma(\Psi)$, as

$$\Gamma(\Psi) = \frac{\partial \Theta_H(\Psi)}{\partial \Psi} = nm\alpha^*(\alpha^*|\Psi|)^{n-1}[1 + (\alpha^*|\Psi|)^n]^{-(m+1)} \tag{4b}$$

where $\alpha^* = \alpha_c/\alpha_{\mathrm{PWC}}$ is the dimensionless inverse capillary length for a given hysteretic moisture-retention branch c. Figure 1 depicts a typical closed-loop hysteresis diagram, in which the PWC and MDC form the bounding curves. We also define α_H^* as the maximum hysteresis loop size given by the ratio of α_{MDC} to α_{PWC}. For nonhysteretic cases the PWC and MDC are the same, and $\alpha_H^* = 1$.

The domain along with the initial and boundary conditions are graphically presented in Figure 2. The dimensionless domain sizes in the horizontal and vertical directions, respectively, are given by $L^* = \alpha_{\mathrm{PWC}}L$ and $H^* = \alpha_{\mathrm{PWC}}H$ with $L[L]$ and $H[L]$ representing the horizontal and vertical domain width and height, respectively. To initialize the problem, we place the entire domain on the PWC and specify a uniform saturation Θ_i. We use flux boundary conditions on all sides, with zero flux applied to the left ($\eta = 0$), right ($\eta = L^*$), and bottom ($\xi = -H^*$) boundaries. We also impose a zero flux on

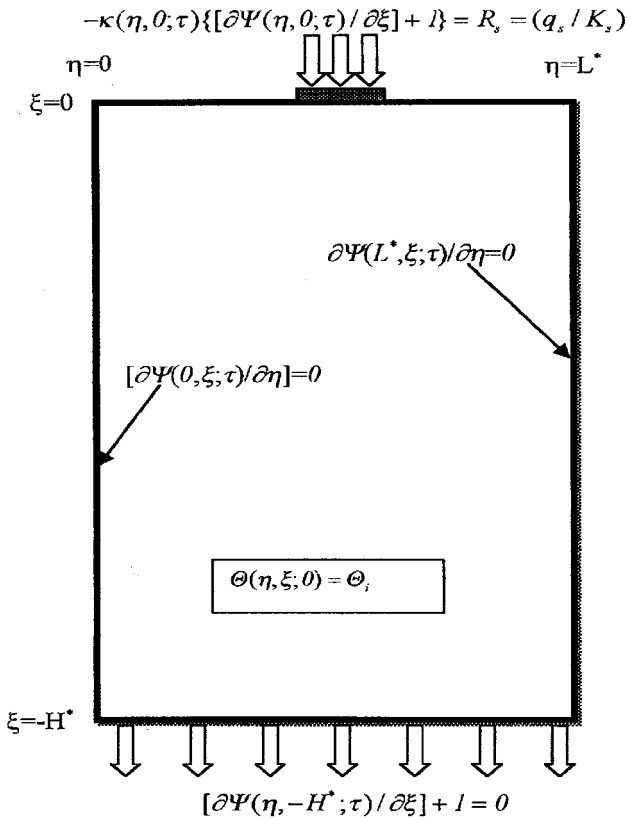

Figure 2. Schematic representation of the computational domain including the initial and boundary conditions.

the top or surface ($\xi = 0$) boundary, except at the center where we supply a constant surface flux ratio of $R_s = q_s/K_s$, over zone of width $(\eta_1 - \eta_0)$. Here $q_s[L/T]$ is the supplied surface flux and $(\eta_1 - \eta_0)$ refers to the dimensionless source width.

As the solution evolves from this initial condition via the imposed flux supplied at the top of the problem, we allow hysteretic property branches as specified by *Scott et al.*'s [1983] hysteresis model to be initiated at any location where a pressure reversal is determined to occur. Thus, from the initial condition on the PWC, a scanning drainage curve (SDC) can be initiated (see Figure 1) with subsequent reversals to higher-order scanning curves as required.

2.2. Finite-Difference Discretization and Solution of the RE

To numerically solve (3) subject to initial and boundary conditions shown in Figure 2, we evaluate the temporal derivative using a fully implicit first-order backward Euler scheme [e.g., *Celia et al.*, 1990] and approximate the spatial derivatives by a staggered grid (i.e., cell-centered) finite difference method (FDM) [e.g., *Harlow and Amsden*, 1975]. Since the discretization of (3) with nonlinear properties (4) results in a system of nonlinear algebraic equations, we use MPI [*Celia et al.*, 1990] to linearize the system of equations. Details for implementing MPI are given by *Cooley* [1983] and *Celia et al.* [1990]. We also use equal and constant grid spacing $\Delta\eta = \Delta\xi$ throughout the domain. In terms of the MPI method, we express the discretized form of our IBVP as

$$\frac{\Gamma_{i,j}^{\nu+1,\mu}}{\Delta\tau_{\nu+1}}\Delta\Psi_{i,j}^{\mu+1} - \frac{1}{\Delta\eta^2}[\kappa_{i+1/2,j}^{\nu+1,\mu}(\Delta\Psi_{i+1,j}^{\mu+1} - \Delta\Psi_{i,j}^{\mu+1}) - \kappa_{i-1/2,j}^{\nu+1,\mu}(\Delta\Psi_{i,j}^{\mu+1} - \Delta\Psi_{i-1,j}^{\mu+1})] - \frac{1}{\Delta\xi^2}[\kappa_{i,j+1/2}^{\nu+1,\mu}(\Delta\Psi_{i,j+1}^{\mu+1} - \Delta\Psi_{i,j}^{\mu+1}) - \kappa_{i,j-1/2}^{\nu+1,\mu}(\Delta\Psi_{i,j}^{\mu+1} - \Delta\Psi_{i,j-1}^{\mu+1})] = r_{i,j}^{\nu+1,\mu}, \quad (5a)$$

where i and j are the mesh point indexes in the η and ξ directions, respectively, $\nu + 1$ refers to the current (i.e., unknown) time step, μ and $\mu + 1$ indicate the previous and current iteration levels for the MPI step, respectively, $\Delta\tau_{\nu+1}$ is the current time step size, $\Delta\Psi^{\mu+1} = (\Psi^{\nu+1,\mu+1} - \Psi^{\nu+1,\mu})$ is the iteration increment (i.e., the change in the unknown pressure between two consecutive nonlinear iteration steps), and $r_{i,j}^{\nu+1,\mu}$ on the right-hand side (RHS) includes all the known parts that are at the iteration level μ. We can write $r_{i,j}^{\nu+1,\mu}$ as

$$r_{i,j}^{\nu+1,\mu} = \frac{1}{\Delta\eta^2}[\kappa_{i+1/2,j}^{\nu+1,\mu}(\Psi_{i+1,j}^{\nu+1,\mu} - \Psi_{i,j}^{\nu+1,\mu}) - \kappa_{i-1/2,j}^{\nu+1,\mu}(\Psi_{i,j}^{\nu+1,\mu} - \Psi_{i-1,j}^{\nu+1,\mu})] + \frac{1}{\Delta\xi^2}[\kappa_{i,j+1/2}^{\nu+1,\mu}(\Psi_{i,j+1}^{\nu+1,\mu} - \Psi_{i,j}^{\nu+1,\mu}) - \kappa_{i,j-1/2}^{\nu+1,\mu}(\Psi_{i,j}^{\nu+1,\mu} - \Psi_{i,j-1}^{\nu+1,\mu})] + \frac{\kappa_{i,j+1/2}^{\nu+1,\mu} - \kappa_{i,j-1/2}^{\nu+1,\mu}}{\Delta\xi} + \frac{R_{s,B}}{\Delta\xi} - \frac{\Theta_{i,j}^{\nu+1,\mu} - \Theta_{i,j}^{\nu}}{\Delta\tau_{\nu+1}}, \quad (5b)$$

where the first and second group of terms on the RHS of (5b) refer to the discretization of capillary components in the η and ξ directions, respectively, the third term is the discretized form of the gravity component, the fourth term includes the applied flux value for the boundary nodes that are subject to a nonzero R_s only, and the last term is the discretization of temporal derivative that arises from the basic formulation of the MPI and takes advantage of the mass-conservative properties of the mixed form of the RE (for more details, see *Celia et al.* [1990]). In (5a) and (5b) all terms with the exception of the unknown vector $\Delta\Psi_{i,j}^{\mu+1}$ are linearized and thus are known.

To obtain the solution for $\Delta\Psi_{i,j}^{\mu+1}$ at the current MPI iteration level, we invert the resulting coefficient matrix using a Line Relaxation (LR) method [e.g., *Anderson et al.*, 1984, p. 134]. (For one-dimensional (1-D) problems considered in section 3, we use the Thomas algorithm [e.g., *Anderson et al.*, 1984, p. 128] to directly invert the matrix.) Since the LR method includes a relaxation parameter Ω, we determine its size using

$$\Omega = [(1 - \sqrt{1 - \rho_s^2})/(1 + \sqrt{1 - \rho_s^2})], \quad (6a)$$

where ρ_s refers to the spectral radius. We calculate ρ_s as suggested by *Press et al.* [1992, p. 867], which for square grids can be written as

$$\rho_s = \tfrac{1}{2}[\cos(\pi/I) + \cos(\pi/J)], \quad (6b)$$

where I and J are the total number of grid points in η and ξ directions, respectively. Since, in general, $\Omega < 1$, we actually use "underrelaxation" which is often required for the convergence of nonlinear elliptic equations [e.g., *Anderson et al.*, 1984, p. 133]. Additionally, as the grid becomes coarser (i.e., I and J decrease), the value of Ω approaches zero, and we find that convergence can be ensured as long as $0.9 \leq \Omega \leq 0.95$. Thus we constrain the relaxation parameter to always fall within this range. Also, to terminate the LR process, we use a convergence criterion of 10^{-12} based on norm-2 error for $\Delta\Psi_{i,j}^{\mu+1}$.

Following matrix inversion, we check for the convergence of the nonlinear iteration step (i.e., MPI). If the absolute and relative errors in the pressure and saturation between two consecutive iterations is greater than a value of 10^{-6}, we update all properties without checking for the hysteretic state of the moisture retention, and continue to iterate until convergence is obtained. Following convergence of the MPI step, we update $\Theta_H(\Psi)$, $\kappa(\Theta)$, and $\Gamma(\Psi)$ for the current time and advance to the next time cycle. In all simulations presented here, the global mass balance error was found to be on the order of 10^{-7} or smaller.

For hysteretic cases, to assess whether any pressure reversals have occurred at the end of each time step (i.e., following MPI convergence), we check for changes in the nodal pressures from the previous time step (i.e., $\Delta\Psi_{i,j}^{\nu+1} = \Psi_{i,j}^{\nu+1} - \Psi_{i,j}^{\nu}$). If the sign of $\Delta\Psi_{i,j}^{\nu+1}$ at node (i, j) has changed, and $|\Delta\Psi_{i,j}^{\nu+1}| > \varepsilon_H$, where ε_H is the reversal threshold, node (i, j) is placed on a new branch. *Kool and Parker* [1987] suggest taking ε_H large enough to avoid the influence of oscillations in the numerical solution. Because we are interested in the influence of the numerical technique, we set ε_H to a small number slightly larger than the computer's round-off error (e.g., $\varepsilon_H \approx 10^{-15}$).

From (5a) and (5b) the numerical parameters controlling the solution are the time step size ($\Delta\tau_{\nu+1}$), spatial grid spacing ($\Delta\eta = \Delta\xi$), and internodal averaging technique ($\kappa_{i,j\pm1/2}^{\nu+1,\mu}$ or $\kappa_{i\pm1/2,j}^{\nu+1,\mu}$). We choose to remove direct dependency on time step size by linking it conservatively to the maximum velocity in the problem as follows. We compute the time step as $\Delta\tau_{\nu+1} = \min(1.05\Delta\tau_\nu, \Delta\tau_{\max})$, where $\Delta\tau_\nu$ and $\Delta\tau_{\max}$ are the previous and maximum time step values, and start simulations with a small initial time step size, $\Delta\tau_0 = 10^{-10}$. $\Delta\tau_{\max}$ is calculated as a fraction of the spatial grid spacing using $\Delta\tau_{\max} = 0.1(\Delta/v_{\max})$, where $\Delta = \Delta\eta = \Delta\xi$ and $v_{\max}$ is the dimensionless maximum Darcy velocity (i.e., the ratio of the dimensionless flux to the saturation) within the problem domain. The constant, 0.1, is a time step safety factor to ensure numerical stability; this constant is related to the Courant-Friedrichs-Lewy (CFL) condition commonly used in numerical solutions of advection-dominated flows [e.g., *Anderson et al.*, 1984, p. 75]. If, however, the MPI step fails to converge within eight iterations, we reduce $\Delta\tau_{\nu+1}$ by 25% and begin the time cycle again.

To evaluate the internodal conductivities (i.e., $\kappa_{i,j\pm1/2}^{\nu+1,\mu}$ or $\kappa_{i\pm1/2,j}^{\nu+1,\mu}$), we considered a number of standard averaging methods such as the upwind, harmonic, geometric, arithmetic, as well as other mixed averaging methods suggested by *Haverkamp and Vauclin* [1979] and *Zaidel and Russo* [1992]. Here we present our results using the first-order downwind (DW1), first-order upwind (UW1), arithmetic averaging or second-order centered difference (CD2), and a third-order centered difference (CD3) as these encompass a full range of behavior. We can express the first three methods using a class of averaging methods called the partial donor cell (PDC) method [e.g., see *Harlow and Amsden*, 1975]. The PDC is given by

$$\kappa_{i,j+1/2}^{\nu+1,\mu} = \tfrac{1}{2}[(1 + ws_{i,j+1/2})\kappa_{i,j}^{\nu+1,\mu} + (1 - ws_{i,j+1/2})\kappa_{i,j+1}^{\nu+1,\mu}], \quad (7a)$$

where w is a weighting parameter and $s_{i,j+1/2}$ determines the flow direction. Although the flow direction is usually deter-

Table 1. Dimensionless Physical and Numerical Parameters for 1-D and 2-D Simulations

Parameters Values Common for Both 1-D and 2-D Simulations	
Applied flux ratio R_s	0.1
Material nonlinearity for MDC, n_{MDC}	15 (see hysteresis curves in Figure 1)
Inverse capillary pressure $\alpha_H^* = \alpha_{\mathrm{MDC}}^*/\alpha_{\mathrm{PWC}}^*$	0.5 (hysteretic) and 1.0 (nonhysteretic)
Hysteretic reversal criterion ε_H	10^{-15}
Convergence criterion for MPI	10^{-6}
2-D Simulations	
Initial saturation Θ_i	10^{-10}
Material nonlinearity for PWC, n_{PWC}	15 (see hysteresis curves in Figure 1)
Domain width L^*	10
Domain height H^*	20
Top boundary condition source width $\eta_1 - \eta_0$	0.2
Convergence criterion for LR solver	10^{-12}
Spatial grid spacing $\Delta\eta = \Delta\xi$	
Plates 1a, 1b, 1c, and 1f	0.20 (5,304 nodes)
Plates 1d, 1e, and 1g	0.05 (81,204 nodes)
1-D Simulations	
Domain height H^*	20
Figures 5, 6, and 7	
Initial saturation Θ_i	10^{-10}
Material nonlinearity for PWC, n_{PWC}	15
Spatial grid spacing $\Delta\xi$	0.2 (Figures 5, 6, 7a, and 7b)
Spatial grid spacing $\Delta\xi$	0.2, 0.08, 0.04, 0.02, 0.01 (Figure 7c)
Figure 8a	
Initial saturation Θ_i	10^{-10} through 10^{-2}, 0.075, 0.3, 0.4
Material nonlinearity for PWC, n_{PWC}	15
Spatial grid spacing $\Delta\xi$	0.2
Figure 8b	
Initial saturation Θ_i	10^{-10}
Material nonlinearity for PWC, n_{PWC}	2, 3, 5, 10, 15, 50
Spatial grid spacing $\Delta\xi$	0.2

mined from the nodal velocity [e.g., *Harlow and Amsden*, 1975], we found it more convenient to use the difference in the hydraulic conductivity of two adjacent nodes to define $s_{i,j+1/2}$ as

$$s_{i,j+1/2} = \mathrm{sgn}(\kappa_{i,j}^{\nu+1,\mu} - \kappa_{i,j+1}^{\nu+1,\mu}) = \begin{cases} 1 & \text{if} \quad (\kappa_{i,j}^{\nu+1,\mu} - \kappa_{i,j+1}^{\nu+1,\mu}) \geq 0 \\ -1 & \text{if} \quad (\kappa_{i,j}^{\nu+1,\mu} - \kappa_{i,j+1}^{\nu+1,\mu}) < 0. \end{cases} \tag{7b}$$

For $w = 0$ and 1, PDC yields the CD2 and UW1 methods, respectively, and for $-1 < w < 0$ we have the DW1 method. When $w = -1$ (i.e., full downwind), the numerical solution fails to converge for flow into an initially dry material [e.g., see *Nieber*, 1996]. For this reason, we generally use $-1 < w < 0$ to form DW1. The w values reported by *Nieber* [1996] for his simulations were -0.9, -0.8, -0.7, -0.5, and 0.0. Similar downwind averaging has also been used by *Ritsema et al.* [1998a, 1998b] and *Nguyen et al.* [1999a, 1999b], but they do not state the w values in their studies. The reported value of *Nieber et al.* [2000] to simulate fingers in highly water-repellent sands was $w = -0.95$. The third-order centered difference method (CD3) we use is *Leonard*'s [1979] method:

$$\kappa_{i,j+1/2}^{\nu+1,\mu} = \tfrac{1}{6}[2\kappa_{i,j+1}^{\nu+1,\mu} + 5\kappa_{i,j}^{\nu+1,\mu} - \kappa_{i,j-1}^{\nu+1,\mu}]. \tag{7c}$$

Finally, note that in (7a), (7b), and (7c) we only state the average between nodes (i, j) and $(i, j + 1)$, that is, $\kappa_{i,j+1/2}^{\nu+1,\mu}$, and thus the same approach must be applied to the other node combinations as well.

2.3. Two-Dimensional Illustrative Examples

Our dimensionless problem statement and numerical solution reduces problem parameters to the material properties (α_H^* and n_{PWC}), initial and boundary conditions (Θ_i and R_s), grid spacing ($\Delta\xi = \Delta\eta$), and choice of averaging method (UW1, DW1, CD2, and CD3). We now present a suite of 2-D simulations that illustrate numerical solution behavior for a single set of physical parameters defined to be within the range where gravity-driven fingers have been found experimentally. We first consider the effect of averaging method for hysteretic simulations with a grid spacing of $\Delta\eta = \Delta\xi = 0.2$, typical of that used by *Nieber* [1996]. We then extend these results and show the effect of grid refinement on the solution by setting $\Delta\eta = \Delta\xi = 0.05$ (i.e., a factor of 4 smaller). Finally, we show two typical nonhysteretic simulations for these two different grid resolutions.

Table 1 summarizes the various physical and numerical problem parameters for the 2-D simulations presented in this section. The computational domain is formed by a rectangle of size $L^* = 10$ by $H^* = 20$. For hysteretic simulations we take $\alpha_H^* = 0.5$, which is representative of many porous materials [e.g., *Kool and Parker*, 1987] as well as sands where gravity-driven fingering occurs (see data by *Norton* [1995]). The value for the media nonlinearity parameter, $n_{\mathrm{PWC}} = 15$, is well within the range for materials that support gravity-driven fingers [e.g., *Norton*, 1995; *Nieber*, 1996; *Ritsema et al.*, 1998a; *Nieber et al.*, 2000]. The initial condition is taken as air dry with a value for Θ_i of 10^{-10}. Finally, the flux in the middle of the top boundary is prescribed by an $R_s = 0.1$, within the range shown by *Glass et al.* [1989a, 1989b, 1989c] to yield fingers.

Plates 1a, 1b, and 1c illustrate typical hysteretic results for the various averaging methods at grid spacing $\Delta\eta = \Delta\xi = 0.2$. The CD2 result (i.e., $w = 0$) in Plate 1a is also representative of both UW1 and CD3 (not shown) and depicts the expected result from the RE with a slender, diffusive plume

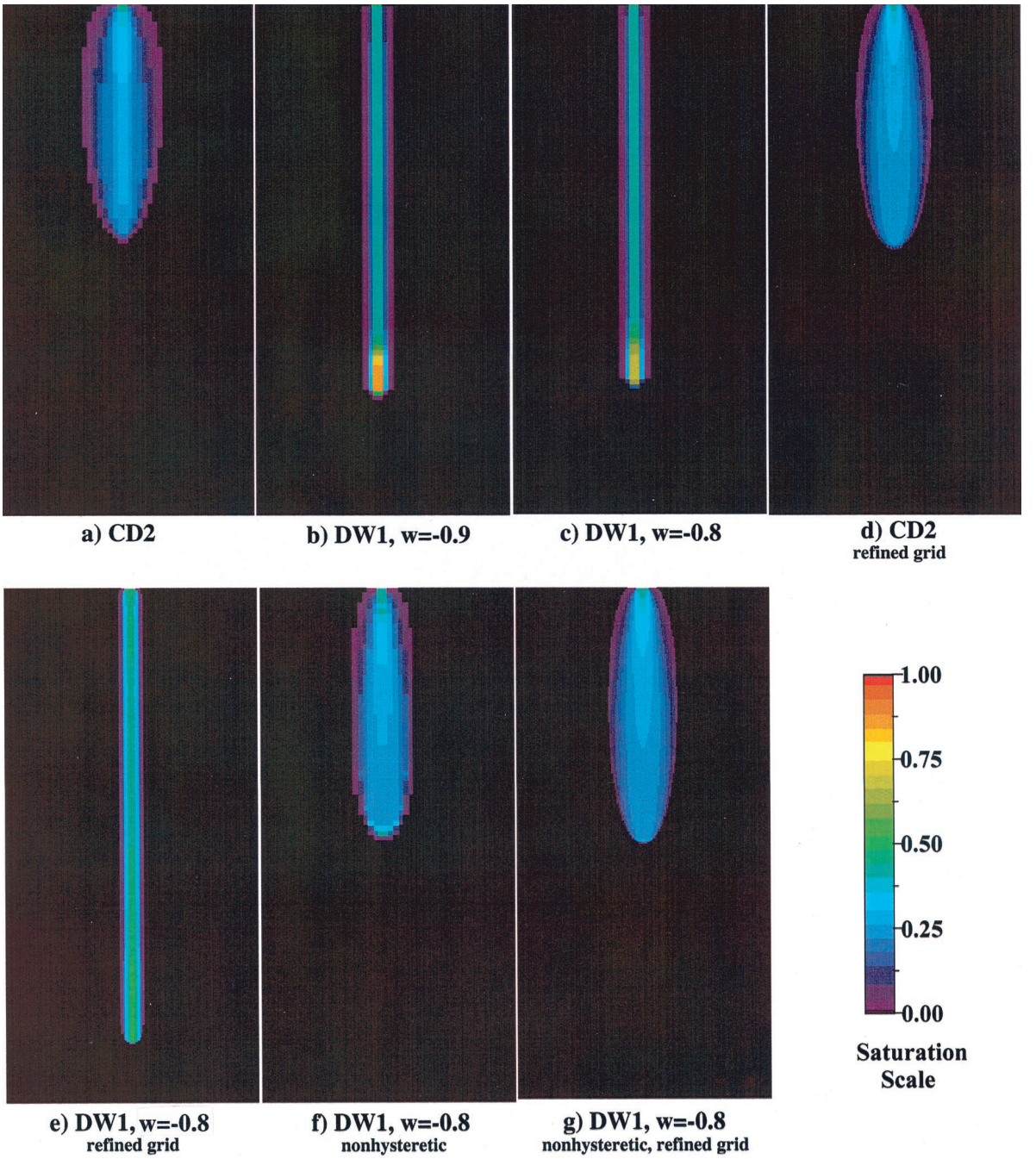

Plate 1. The 2-D RE simulations for constant flux infiltration in an initially dry media at $\tau = 100$ (see Table 1 for physical parameter values). Each image has a dimensionless height of 20 and width of 10, and the saturation of each grid block is depicted with a color scale that ranges from zero to one without interpolation or smoothing. Hysteretic results for grid spacing $\Delta\eta = \Delta\xi = 0.2$: (a) CD2, (b) DW1 with $w = -0.9$, and (c) DW1 with $w = -0.8$. Effect of grid refinement on hysteretic cases for $\Delta\eta = \Delta\xi = 0.05$: (d) CD2 and (e) DW1 with $w = -0.8$. Nonhysteretic results for DW1 with $w = -0.8$ for two different grid spacings: (f) $\Delta\eta = \Delta\xi = 0.2$, and (g) $\Delta\eta = \Delta\xi = 0.05$.

growing both downward and laterally. We note that for these simulations, no hysteretic reversals occurred. DW1 results with $w = -0.9$ and -0.8 are shown in Plates 1b and 1c, respectively. The values for the w parameter selected for these simulations are typical of those reported by *Nieber* [1996]. The DW1 results are qualitatively similar to a physical finger and demonstrate a hysteretic reversal with higher-saturation finger tips that drain a distance behind. Vertical saturation profiles along the centerline for each of these fields (Figure 3a) show clearly that while the saturation for the CD2 simulation is monotonic with the maximum saturation occurring near the source (i.e., at $\xi = 0$), the DW1 profiles are nonmonotonic with the maximum saturation occurring at the finger tip. Also, note in Figure 3a that, for $w = -0.9$, the maximum saturation at the finger tip is ~0.88, while for $w = -0.8$ it reduces to ~0.70. In other words, we see that a small increase in the w value,

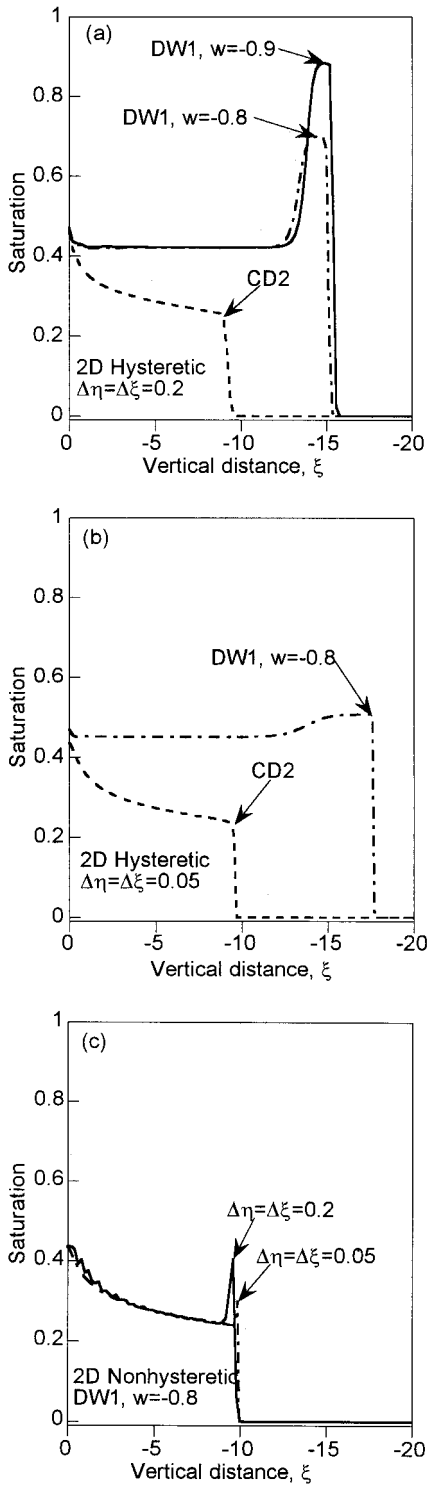

Figure 3. Vertical saturation profiles along the centerline $\eta = 5$ for the various 2-D results shown in Plate 1: (a) hysteretic cases for $\Delta\eta = \Delta\xi = 0.2$ shown in Plates 1a, 1b, and 1c, (b) hysteretic cases for $\Delta\eta = \Delta\xi = 0.05$ shown in Plates 1d and 1e, and (c) nonhysteretic cases shown in Plates 1f and 1g.

which is simply a numerical parameter, has a significant influence on the finger tip saturation.

The differences in the solution results for DW1 and the other averaging methods (as represented by CD2) are striking. What is the cause? A first hint is found when we consider grid spacing. Reducing the grid spacing by a factor of 4 to $\Delta\eta = \Delta\xi = 0.05$ and repeating the calculations shows the solution for CD2 (as well as UW1 and CD3, again not shown here) to change only slightly (Plate 1d) indicating that we are indeed at or very near the converged (i.e., grid-independent) solution of the RE. However, for DW1 with $w = -0.8$, as we refine the grid, we find that the finger core begins to slightly widen (Plate 1e), and as Figure 3b reveals, the maximum saturation at the finger tip is now decreased from ~0.70 for $\Delta\eta = \Delta\xi = 0.2$ to ~0.51 for $\Delta\eta = \Delta\xi = 0.05$. Thus, as we refine the grid, the nonmonotonic signature of the gravity-driven finger fades. A second hint arises when we consider nonhysteretic solutions. Plates 1f and 1g depict the nonhysteretic solutions for DW1 with $w = -0.8$, using $\Delta\eta = \Delta\xi = 0.2$ and $\Delta\eta = \Delta\xi = 0.05$, respectively. The solutions for the nonhysteretic cases are now more diffuse and closer to the CD2 results. However, under close scrutiny these solutions show a one node long "oscillation" or oversaturation at the advancing tip of the profile (see Figure 3c). Such an oscillation does not occur for similar nonhysteretic solutions with CD2, UW1, or CD3.

As we will show in the next section, the ability of DW1 to simulate fingers is wholly due to the oscillation or oversaturation at the WF seen in the nonhysteretic case. We will also show the oscillation arises from the LTE terms of the spatial (i.e., capillary and gravity) components of the RE, whose functional behavior and magnitude are directly related to the averaging method used. In combination with hysteresis this local numerical oscillation yields an "organized oscillation" with a wavelength ~0.5 (i.e., $\sim\alpha_H^*$) similar to that found for physical fingers [*Glass et al.*, 1989b]. We shall also show this finger-like behavior in our 2-D illustrations for DW1 but not for CD2 (or UW1 and CD3) is caused by the fact that, at the grid spacing used, the LTE terms for DW1 are more than 1 order of magnitude larger than for CD2. Thus the 2-D numerical solutions using DW1 are not solving the RE at all, but a modified governing equation where the truncation error yields artificial terms that are of comparable size to the physical components in the RE.

3. Truncation Error and the Modified Governing Equation

Formal evaluation of the local truncation error is conducted by Taylor series expansion of each term in the discretized equation. Following the Taylor series expansion, we obtain an equation that is composed of the original PDE along with other additional terms. This equation, referred to as the "modified governing equation," is the actual PDE being solved [*Warming and Hyett*, 1974]. Appendix A presents the power series forms of the local truncation error terms for temporal, capillary, and gravity components in the RE as a function of the various averaging methods used in this study. In general, the leading (i.e., the lowest order) terms for each of the power series are largest, yielding the following lowest-order, modified governing equation for constant grid spacing:

$$\Gamma(\Psi)\frac{\partial\Psi}{\partial\tau} - \left\{\frac{\partial}{\partial\eta}\left[\kappa(\Psi)\frac{\partial\Psi}{\partial\eta}\right] + \frac{\partial}{\partial\xi}\left[\kappa(\Psi)\frac{\partial\Psi}{\partial\xi}\right]\right\} - \frac{\partial\kappa(\Psi)}{\partial\xi} = -\Gamma(\Psi)\left(\frac{\Delta\tau}{2}\right)\frac{\partial^2\Psi}{\partial\tau^2} - E_{\text{cap}}(\eta,\xi) - \beta_\ell\frac{\partial^{\ell+1}\kappa(\Psi)}{\partial\xi^{\ell+1}}. \tag{8a}$$

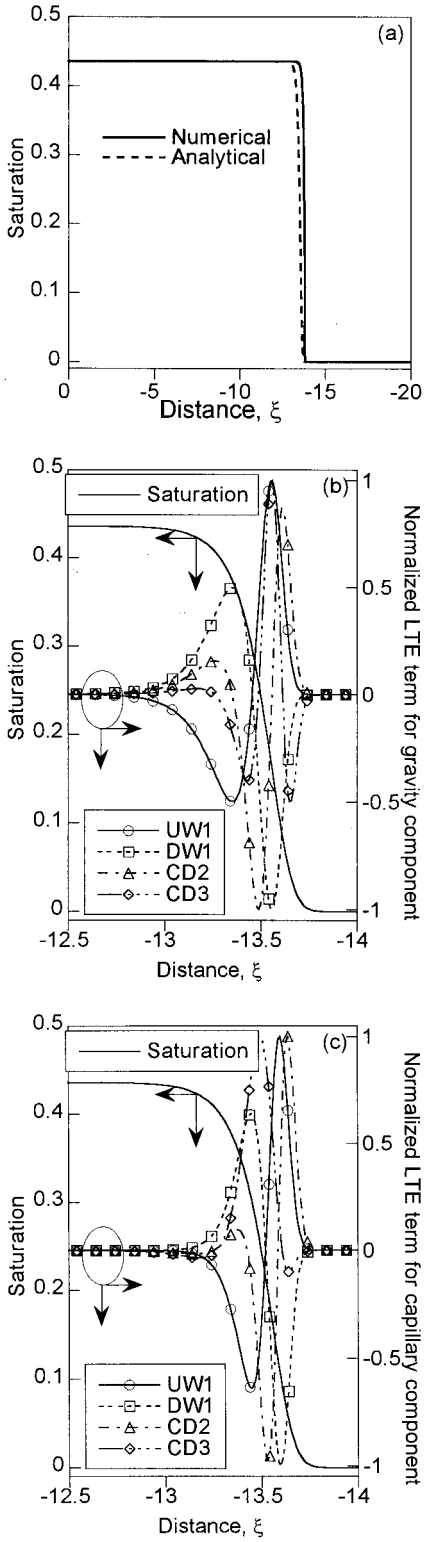

The left-hand side (LHS) of (8a) represents the original form of the RE stated in (3), and the three terms on the RHS refer to the LTE terms for the temporal, capillary, and gravity components, respectively. β_ℓ is the lowest spatial coefficient for each averaging method, and ℓ refers to the spatial order of accuracy of the averaging method. For the averaging methods considered here: $\ell = 1$ and $\beta_\ell = w(\Delta\xi/2)$ for UW1 ($w = 1$) and DW1 ($w < 0$); $\ell = 2$ and $\beta_\ell = \Delta\xi^2/6$ for CD2; and finally for CD3, $\ell = 3$ and $\beta_\ell = \Delta\xi^3/12$.

Using Appendix A, the capillary component's LTE term $E_{\text{cap}}(\eta, \xi)$ for the first-order methods DW1 and UW1 (i.e., $\ell = 1$) can be written as

$$E_{\text{cap}}(\eta, \xi) = w\left\{\left(\frac{\Delta\eta}{2}\right)\frac{\partial}{\partial\eta}\left[\frac{\partial\Psi}{\partial\eta}\frac{\partial\kappa(\Psi)}{\partial\eta}\right] + \left(\frac{\Delta\xi}{2}\right)\frac{\partial}{\partial\xi}\left[\frac{\partial\Psi}{\partial\xi}\frac{\partial\kappa(\Psi)}{\partial\xi}\right]\right\} \tag{8b}$$

with $w < 0$ for DW1 and $w = 1$ for UW1. For the second-order CD2 method (i.e., $\ell = 2$), $E_{\text{cap}}(\eta, \xi)$ is of the form

$$E_{\text{cap}}(\eta, \xi) = \frac{\Delta\eta^2}{6}\left\{\frac{1}{2}\frac{\partial^2}{\partial\eta^2}\left[\kappa(\Psi)\frac{\partial^2\Psi}{\partial\eta^2}\right] + \frac{\partial}{\partial\eta}\left[\frac{\partial\Psi}{\partial\eta}\frac{\partial^2\kappa(\Psi)}{\partial\eta^2}\right]\right\} + \frac{\Delta\xi^2}{6}\left\{\frac{1}{2}\frac{\partial^2}{\partial\xi^2}\left[\kappa(\Psi)\frac{\partial^2\Psi}{\partial\xi^2}\right] + \frac{\partial}{\partial\xi}\left[\frac{\partial\Psi}{\partial\xi}\frac{\partial^2\kappa(\Psi)}{\partial\xi^2}\right]\right\}, \tag{8c}$$

and lastly for the third-order CD3 method (i.e., $\ell = 3$), $E_{\text{cap}}(\eta, \xi)$ becomes

$$E_{\text{cap}}(\eta, \xi) = \frac{\Delta\eta^2}{12}\left\{2\frac{\partial^3\Psi}{\partial\eta^3}\frac{\partial\kappa(\Psi)}{\partial\eta} + \frac{\partial^2}{\partial\eta^2}\left[\kappa(\Psi)\frac{\partial^2\Psi}{\partial\eta^2}\right]\right\} + \frac{\Delta\xi^2}{12}\left\{2\frac{\partial^3\Psi}{\partial\xi^3}\frac{\partial\kappa(\Psi)}{\partial\xi} + \frac{\partial^2}{\partial\xi^2}\left[\kappa(\Psi)\frac{\partial^2\Psi}{\partial\xi^2}\right]\right\}. \tag{8d}$$

Note that for the CD3, discretization of the capillary component reduces the overall accuracy of the solution to only second order. We also note that when the grid is not uniform, the order of accuracy for all averaging methods also reduces by 1 for both the capillary and gravity components. Regardless, the critical issue is that when the various LTE terms are large enough for the RHS of (8a) to be nonnegligible, the numerical method actually solves a different governing equation than intended.

Figure 4. (opposite) Analytical illustrations of LTE term behavior for the various averaging methods: (a) comparison between the 1-D numerical (solid) and analytical (dashed) profiles; and normalized LTE term behavior for the (b) gravity component and (c) capillary component. The numerical profile in Figure 4a is the converged solution for UW1 with $n = 15$, $\Delta\xi = 0.01$ and other parameters listed in Table 1. Equation (9) approximates the numerical solution with $\Psi_A = -5.1795$, $\Psi_i = -1.0244$, $\xi_{WF} = -14$, and $\lambda = 115$. The saturation profile shown in Figure 4a is obtained by substituting (9) into (4a) with $n = 15$ and $\alpha^* = 1$. The LTE terms are evaluated analytically using (8a) through (8d). The magnitude of the truncation error terms (on the right-hand vertical axis) are normalized by their maximum (i.e., infinite norm) values to facilitate behavioral comparison.

In the remainder of this section we analyze the behavior of the spatial LTE terms with special emphasis near the WF. Because we use a very restrictive CFL-based time step criterion, the temporal LTE term is always negligibly small and thus is not discussed further in this paper. To make our analysis more tractable, we first focus on a 1-D vertical problem where all η terms drop. In section 3.1 we illustrate and categorize the qualitative behavior of the various LTE terms (equations (8a) through (8d)) using a hypothetical, 1-D analytic representation for the pressure head profile across a WF. To fully consider the magnitudes of the LTE terms and their feedback within the RE, we next present a series of nonhysteretic and hysteretic 1-D simulations in sections 3.2 and 3.3, respectively, and evaluate numerical representations of the various LTE terms. These 1-D numerical results, while approximate, allow us to quantitatively discuss the behavior of the various LTE terms and their role in yielding oscillatory behavior. In particular, when hysteresis is included, the LTE terms are shown to cause an organized oscillation that is quite similar to the nonmonotonic profile within a physical gravity-driven finger. Interestingly, in section 3.4 we illustrate additional near physical trends in the 1-D finger-like solutions as a function of the initial saturation and material nonlinearity. Finally, in section 3.5 we analyze the behavior of the LTE terms in 2-D solutions and relate the origin of the 2-D finger-like response to the oscillations seen in the 1-D cases.

3.1. One-Dimensional Analytical Illustration of LTE Term Behavior

To illustrate the functional behavior of the various spatial LTE terms across the WF, we consider a hypothetical pressure profile

$$\Psi(\xi) = (\Psi_A - \Psi_i)\left\{ \exp\left(-\frac{\xi}{\xi_{WF}} \right)^{\lambda} - 1 \right\} + \Psi_A, \qquad (9)$$

where Ψ_A is the final or asymptotic pressure, Ψ_i is the initial pressure, ξ_{WF} is a scaling parameter that is used to adjust the WF position, and λ is a WF sharpness factor. The profile (9) is not a solution of the RE; however, it qualitatively adheres to such solution profiles (see Figure 4a) and allows us to analytically consider and categorize the fundamental qualitative behaviors of each LTE term as a WF is crossed. Substituting (9) into (4a) yields saturation $\Theta(\xi)$ and hydraulic conductivity $\kappa(\xi)$ profiles, which are then explicitly evaluated for the various spatial derivatives on the RHS of (8a) through (8d).

Figures 4b and 4c show the functional behavior of the gravity and capillary components' LTE terms for the different averaging methods, plotted along with the hypothetical saturation profile $\Theta(\xi)$ near the WF. In order to focus on the behavior across the WF the values for the LTE terms in this figure are normalized so that they range between -1 and $+1$. For UW1 the LTE term for the gravity component has a second derivative of κ with respect to ξ which, as Figure 4b shows, yields a positive maximum and a negative minimum ahead and behind the WF, respectively. For DW1 the form of this error is identical to that of UW1 with $w < 0$. Thus DW1's behavior is opposite to that of UW1 as the WF is crossed. Since CD2 (i.e., $w = 0$) has a third-order derivative, with respect to UW1, CD2 naturally yields another peak further behind the WF (see Figure 4b). Finally, for CD3 the fourth-order derivative yields yet an additional valley ahead of the WF. For the capillary component the LTE term behavior is less obvious from (8b) through (8d). However, we see in Figure 4c that normalized $E_{\mathrm{cap}}(\xi)$ profiles for UW1, DW1, and CD2 all display a similar behavior to their gravity component LTE terms, and thus are in phase across the WF.

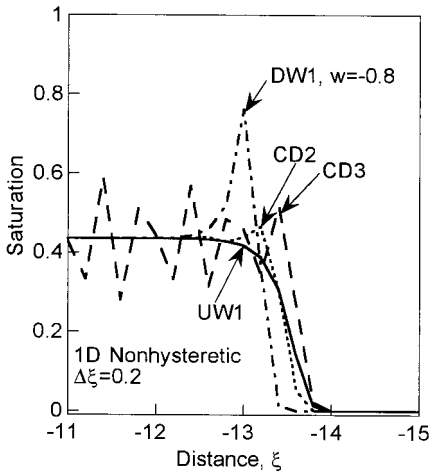

Figure 5. Nonhysteretic 1-D saturation profiles near the wetting front as a function of averaging technique at $\tau = 60$ for $\Theta_i = 10^{-10}$, $R_s = 0.1$, $n_{\mathrm{PWC}} = 15$, and $\Delta\xi = 0.2$.

We can categorize the various methods with respect to their LTE term behavior as follows. UW1 yields an "artificial diffusion," which speeds up the "front" of the WF and slows down its "back," the net effect being to smear the WF [e.g., *Gresho and Lee*, 1981]. Because of this behavior across the WF, UW1 is inherently monotonic [e.g., see *Forsyth and Kropinski*, 1997]. Since the LTE terms for DW1 are opposite of UW1, DW1 yields an "artificial compression," which holds back the front of the WF and speeds up its back, the net effect being to sharpen the WF [*Leonard and Niknafs*, 1991]. The positive error behind the WF can ultimately cause an oversaturation and thus a nonmonotonic response. For both CD2 and CD3 the LTE term behavior, in general, yields an "artificial dispersion," which distorts a WF by introducing oscillations [e.g., see *Anderson et al.*, 1984, p. 92; *Patel et al.*, 1985; *Liu et al.*, 1995; *Forsyth and Kropinski*, 1997]. As with DW1, the positive portions of the oscillatory error behind the WF can cause corresponding oversaturation and nonmonotonicity for these methods. Finally, this analysis allows one to easily understand the influence of WF sharpness on the LTE terms. As λ increases and the WF sharpens (i.e., as the gradients in pressure, saturation, and hydraulic conductivity across the WF grow), the LTE terms focus to a narrowing zone near the WF where their absolute values (both negative and positive) will grow. In general, such WF sharpening corresponds to increases in media nonlinearity n or decreases in the initial saturation Θ_i.

3.2. One-Dimensional Nonhysteretic Simulations and LTE Term Behavior

To consider the quantitative behavior of each LTE term in the context of the numerical solution where feedback among the various terms occurs, we solve the 1-D problem for the same set of physical parameters used in our 2-D illustrations in section 2.3 with numerical parameters as listed in Table 1. Figure 5 presents near WF saturation profiles for the various averaging methods at a grid spacing of $\Delta\xi = 0.2$. Not surprisingly, while only UW1 attains a monotonic (i.e., oscillation-

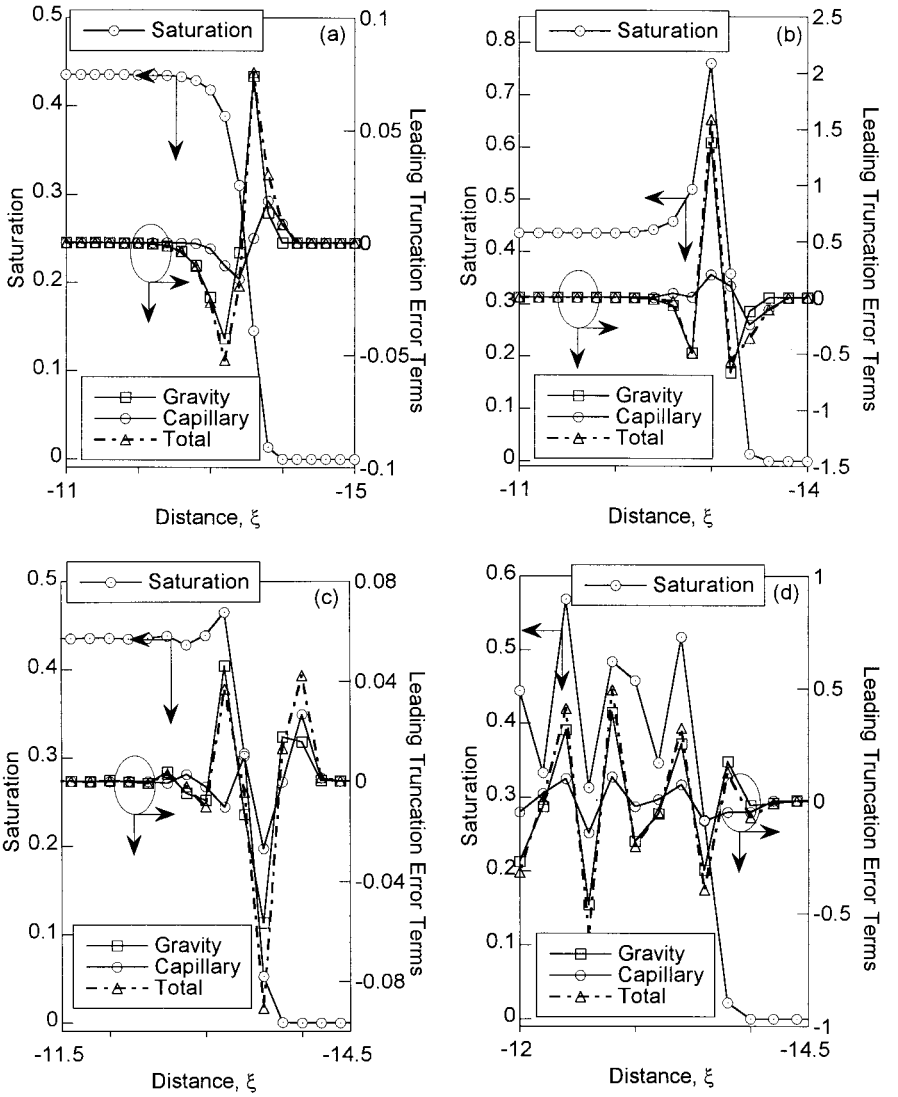

Figure 6. Saturation profiles (see left-hand vertical axis) along with the local behavior of the gravity, capillary, and total LTE terms (see right-hand vertical axis) for 1-D nonhysteretic results shown in Figure 5: (a) UW1, (b) DW1 with $w = -0.8$, (c) CD2, and (d) CD3. Note that to focus on the behavior near the WF, the vertical scales among the figures are different.

free) solution, all other averaging methods yield oscillatory results. The oscillatory nature of each profile depends upon the averaging technique used. DW1 and CD2 show a single oscillation of different amplitude at the back of the WF, but for CD3, oscillations of varying periodicity and amplitude persist over the entire domain behind.

Figure 6 displays the behavior of the gravity, capillary, and total LTE terms for each of the profiles in Figure 5. To calculate the LTE terms, we use the forms on the RHS of (8a) through (8d) and employ second-order centered differences to numerically estimate the various spatial derivatives from the profiles. (We found centered differences to preserve symmetry in the 1-D analytical illustrations presented in section 3.1 and in the 2-D analysis presented later in section 3.5). Thus the LTE terms are evaluated posteriori at the end of the simulations using the computed nodal pressure, saturation, and hydraulic conductivity values.

In the case of UW1 (Figure 6a) the forms of the LTE term for the gravity and capillary components are similar to the analytical illustrations; that is, both LTE terms have a positive and then a negative value ahead and behind the WF, respectively. Across the WF the LTE term behavior for the other three averaging methods is also consistent with the analytical illustrations; however, we also see additional features. For the DW1 method (Figure 6b) we find an additional negative error swing behind the WF. For CD2 (Figure 6c), also at the back of the WF, the LTE terms for the capillary and gravity components are out of phase. Finally, as Figure 6d displays, the LTE terms for CD3 continue to oscillate behind the WF. However, despite these differences, at the WF where we are most interested, the LTE terms for the capillary and gravity components are in phase for all methods and behave similarly to the analytical illustrations presented in section 3.1 and shown in Figures 4b and 4c.

It is clear from Figure 6 that the oversaturation behind the WF for DW1, CD2, and CD3, or the lack thereof for UW1, is due to the magnitude and behavior of the LTE terms as the WF is crossed. DW1 exhibits the largest LTE term magnitude

and corresponding oversaturation, followed by CD3, and CD2. In the case of CD2 the oscillation due to the LTE terms does not result in a very large oversaturation because CD2's LTE terms are more than an order of magnitude smaller than that of DW1 (compare the LTE term values at the WF between Figures 6b and 6c). Comparison of DW1 and UW1, which have opposite LTE term functionality across the WF, emphasizes the positive feedback within DW1 to increase and negative feedback within UW1 to decrease the local truncation error. For DW1 the WF is sharpened by the LTE terms which in turn increases their magnitude; while for UW1 the LTE terms smear the WF and thereby decrease their magnitude. Finally, for all averaging methods, Figure 6 also shows the magnitude for the gravity component's LTE term is on average larger than the LTE term for the capillary component, but both are always of the same order of the magnitude.

3.3. One-Dimensional Hysteretic Simulations and LTE Term Behavior

If we now consider the hysteretic solution for the same 1-D cases as presented in section 3.2, we find an oscillatory structure which, as shown in Figure 7a, is entirely different from the nonhysteretic profiles. While the solution for UW1 is once again monotonic and is indeed the same as the nonhysteretic case, the profiles for the other averaging methods now exhibit an "organized oscillation," with a wavelength an order of magnitude longer than that typical of the nonhysteretic oscillations. The amplitude of the organized oscillation (i.e., the saturation at the back of the WF) varies as a function of the averaging method and is directly related to the magnitude of the LTE term. The DW1 method has the highest peak saturation value, followed by CD3 and CD2. An example of the LTE term behavior for DW1 with $w = -0.8$ is presented in Figure 7b. Comparison of Figure 7b to Figure 6b shows only a slight difference in form and magnitude between hysteretic and nonhysteretic cases. This is illustrative of what we find for the other averaging methods (i.e., UW1, CD2, and CD3) as well.

The formation of the organized oscillation is explained through the interaction of the LTE terms and hysteresis. From Figure 1 we can see that a small change in the pressure at the WF corresponds to a large change in saturation on the PWC. The negative and positive swings in the spatial LTE terms for all methods but UW1 cause the WF to first sharpen and then overshoot the pressure/saturation at the back of the WF. For nonhysteretic cases, where saturation is evaluated using the PWC, the next downswing of the LTE terms behind the WF yields a downward oscillation in saturation of short wavelength. However, when hysteresis is considered and the downswing in the computed pressure behind the WF satisfies the reversal threshold ε_H, the pressure oscillation causes a false reversal to a new SDC. Referring to Figure 1, we see that the dimensionless pressure downswings must be ~0.5 (i.e., on the order of α_H^*) on the SDC before they substantially influence the saturation behind the WF. While additional oscillations behind the WF can cause reversals to secondary and higher-order scanning (wetting or drainage) curves, the functional behavior of these curves significantly masks the influence of the small pressure perturbations on the saturation profile. Thus hysteresis in combination with LTE term-induced numerical oscillation yields an organized oscillation with a wavelength on the order of α_H^*, similar to that found for physical gravity-driven fingers [*Glass et al.*, 1989b].

Finally, it is important to realize that, as we reduce the grid

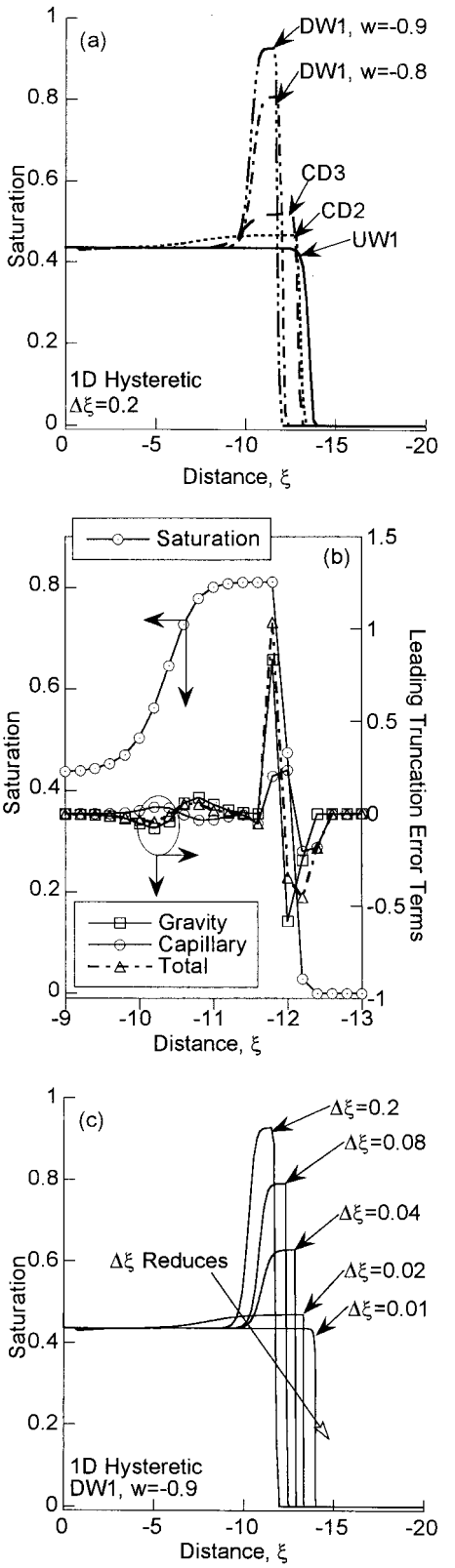

Figure 7. One-dimensional hysteretic saturation profiles: (a) saturation profiles as a function of averaging technique for the identical problem shown in Figure 5, (b) saturation profiles plotted along with the gravity, capillary, and total LTE terms for DW1 with $w = -0.8$, and (c) the effect of grid refinement for DW1 with $w = -0.9$.

spacing, we decrease the LTE terms and eventually obtain a "converged" (i.e., grid-independent) solution. To illustrate the effect of grid refinement, Figure 7c presents the trend in the 1-D hysteretic simulations with $\Delta\xi$ for the case with the largest organized oscillation (DW1 with $w = -0.9$). As $\Delta\xi$ becomes smaller, the amplitude of the organized oscillation behind the WF diminishes yielding a converged, oscillation-free solution that is monotonic for $\Delta\xi = 0.01$. This same trend toward monotonicity with decreasing $\Delta\xi$ is also observed for CD2 and CD3; however, convergence is obtained much sooner due to their smaller LTE terms.

3.4. Near Physical Trends in Organized Oscillation With Initial Saturation and Media Nonlinearity

While not fully understood, both the initial saturation and media nonlinearity have been found to influence the occurrence and behavior of physical gravity-driven fingers [*Glass and Nicholl*, 1996]. As the initial saturation increases, fingers widen and eventually are suppressed. With respect to media nonlinearity, fingers have been found in sands where n_{PWC} is large but not in soils where n_{PWC} is small. Interestingly, for a given $\Delta\xi$ where the LTE terms are prominent, the influences of the initial saturation Θ_i and material nonlinearity n_{PWC} on numerical oscillation are similar to their effects on physical gravity-driven fingers. That is, as the WF sharpness decreases due to an increase in Θ_i or a reduction in n_{PWC}, the strength of numerical oscillations diminishes.

As an illustration of this near physical behavior, we present 1-D hysteretic solutions for $\Delta\xi = 0.2$ using DW1 ($w = -0.8$ and $R_s = 0.1$), for $n_{\mathrm{PWC}} = 15$ and various Θ_i values in Figure 8a, and various n_{PWC} values with $\Theta_i = 10^{-10}$ in Figure 8b. In Figure 8a we see that, for the chosen $\Delta\xi$ and for n_{PWC}, the initial saturation has no effect on the final solution over the range from $10^{-10} \leq \Theta_i \leq 10^{-2}$, but for larger Θ_i values the amplitude of the organized oscillation (i.e., the saturation behind the WF) drops and the WF position moves further into the domain. Eventually, for Θ_i of 0.4 (just below the value determined by the top flux boundary condition) the solution is monotonic. Considering media nonlinearity in Figure 8b, for a medium with $n_{\mathrm{PWC}} \leq 2$ where the WF is naturally nonsharp (e.g., soils), the LTE terms are small, and we obtain an oscillation-free solution. However, as n_{PWC} increases and the WF sharpens, the organized oscillation grows because the greater gradient across the WF results in larger LTE terms.

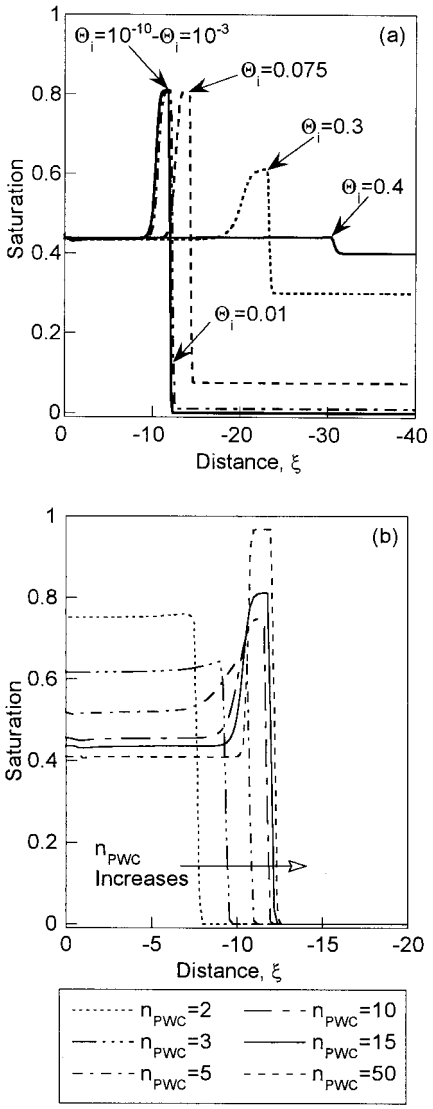

Figure 8. Hysteretic 1-D saturation profiles for DW1 with $w = -0.8$, $\Delta\xi = 0.2$, and $R_s = 0.1$: (a) $n_{\mathrm{PWC}} = 15$ and various Θ_i values (note the domain size has been extended so that the bottom no flux boundary condition does not influence the WF at higher Θ_i values); and (b) $\Theta_i = 10^{-10}$ and various n_{PWC} values (note for a given R_s, different n_{PWC} values result in different saturation values behind the WF).

3.5. Role of LTE Term Behavior in "Simulating" Fingers in Two Dimensions

We now return to analyze the LTE term behavior for representative 2-D hysteretic and nonhysteretic simulations. Here we will first focus on the DW1 method because DW1 yielded 2-D finger-like solutions (section 2.3) while the other averaging methods (e.g., CD2) did not. To calculate an LTE term field, we again use the derivatives stated in the RHS of (8a) and (8b) and employ central differences to numerically estimate the LTE terms from the 2-D solution field. This procedure is the same as that used for the 1-D nonhysteretic and hysteretic cases (sections 3.2 and 3.3) extended to 2-D. The total LTE term fields for the 2-D simulations shown in Plate 1c (hysteretic) and Plate 1f (nonhysteretic) yield a much more complicated error field than those in 1-D. In order to present the total LTE term graphically, we assign black, white, and gray shades to regions with negative, positive, and zero total LTE term, respectively, in Figures 9a and 9b. We see that as the WF is crossed either in the vertical or horizontal, the total LTE term varies from negative to positive and back to negative. Thus the overall error behavior is consistent with our previously discussed 1-D findings. The total LTE term for the nonhysteretic case (Figure 9b) also shows additional oscillations behind the front up through the center of the saturation plume (as can also be seen in Figure 3c). Vertical profiles along the centerline of the fields near the WF for the saturation and the gravity, capillary, and total LTE terms are shown in Figures 10a and 10b. The behavior of these profiles again is consistent with the hysteretic and nonhysteretic 1-D results. Thus the negative part of LTE terms (ahead of the WF) sharpens the WF, while the positive portion (behind the WF) generates an oscillation and thus an oversaturation. Comparison of Figures 10a with 7b shows that the magnitude of the LTE term for the hysteretic 2-D and 1-D cases are both nearly the same. However, a

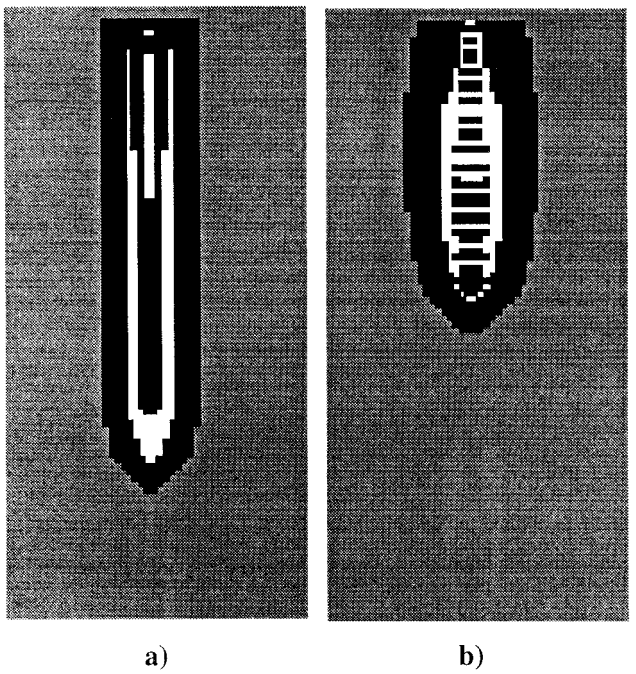

Figure 9. Two-dimensional total LTE term fields for DW1 with $w = -0.8$ and $\Delta\eta = \Delta\xi = 0.2$: (a) hysteretic simulation in Plate 1c and (b) nonhysteretic simulation in Plate 1f. Positive, negative, and zero values of the total LTE terms are mapped with black, white, and gray shades, respectively, to show the general oscillatory solution behavior.

similar comparison of nonhysteretic cases (Figures 10b and 6b) shows the LTE term magnitude in 2-D to be approximately a third of that in 1-D. The more diffuse nature of the 2-D nonhysteretic solution is directly attributable to this reduction in LTE term magnitude.

As a final analysis of tying the LTE terms to finger-like behavior from the RE, we were curious why CD2 did not yield a 2-D finger-like response in our earlier simulation (Plate 1a). On the basis of our current understanding, when the LTE term is sufficiently large (e.g., due to a very large grid spacing), any averaging method with an oscillatory behavior should be able to yield a finger-like solution with its nonmonotonic signature. We therefore considered a case using CD2 where $\Delta\eta = \Delta\xi = 1.0$, with the source two nodes wide and all other problem parameters identical to the ones used in Plate 1a. The simulation indeed yields a finger-like solution with a width two nodes wide and a nonmonotonic organized oscillation with a maximum saturation of ~0.50 at the finger tip draining to ~0.43 behind). Thus, by increasing the grid spacing and the magnitude of the corresponding LTE terms, CD2 can indeed yield a finger-like behavior in 2-D.

4. Discussion

Our analysis of the numerical solution of the RE supports our thesis that the RE with standard monotonic properties does not incorporate the critical physics required to model gravity-driven fingers and must be considered inadequate within the range of parameter space where such fingers occur. In the following, we consider three general points of discussion that address the applicability of the traditional RE. The first considers issues surrounding the comprehensiveness of our numerical results. The second asks whether the traditional full two-phase flow approach would be able to simulate gravity-driven fingers while the RE cannot. The third addresses the artificial alteration of standard monotonic property parameters and, in particular, the artificial reduction in the capillary pressure driving the flow through scaling of α_{PWC}.

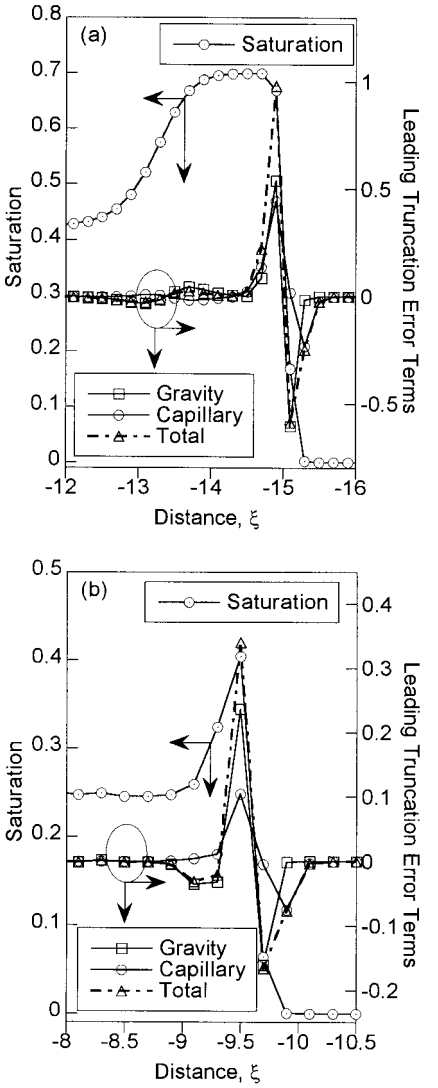

Figure 10. Vertical transects along the axis of symmetry $\eta = 5$ of saturation (see left-hand vertical axis) and the gravity, capillary, and total LTE terms (see right-hand vertical axis) for: (a) hysteretic simulation in Plate 1c and (b) nonhysteretic simulation in Plate 1f.

4.1. Additional Numerical Experiments

The RE along with standard monotonic properties yields a fairly complicated and nonlinear set of equations; only approximate analytical solutions can be found, thus forcing us to use numerical solutions. Because we argue in this paper that this set of equations does not produce fingers where they have shown to occur both physically [e.g., *Glass et al.*, 1989b] and numerically [e.g., *Nieber*, 1996], we attempted to be as thorough as possible and conducted a number of supporting studies that are not presented in this paper. We performed a wide range of simulations with our numerical code where we care-

fully considered issues of (1) numerical accuracy and requirements for solution monotonicity as a function of various averaging methods; (2) implementation of implicit forms of the Total Variations Diminishing (TVD) technique to ensure monotonic results [*Eliassi and Glass*, 1997]; (3) the influence of the hysteretic reversal threshold; (4) the choice of the capillary hysteresis model [e.g., *Scott et al*., 1983; *Mualem*, 1974, 1984; *Hogarth et al*., 1988]; and (5) the use of noniterative as well as predictor-corrector time marching methods. Additionally, for both 1-D and 2-D simulations we considered much wider ranges of parameter values (i.e., Θ_i, n_{PWC}, R_s, and α^*) than reported in this paper and also conducted numerical experiments to examine horizontal imbibition, capillary rise, and gravity drainage under both flux and head boundary conditions. All of these supporting studies reinforced the results and conclusions of this paper.

Finally, to confirm our results, we also considered two entirely different numerical solution approaches embodied in codes written by others. First, we implemented the downwind method in the 1-D hysteretic FEM-based HYDRUS [*Kool and van Genuchten*, 1991] code (as opposed to our use of a FDM-based discretization). This approach produced results that were similar to those presented in this paper. That is, the 1-D hysteretic results with HYDRUS also yielded an organized oscillation when the grid was coarse enough and a monotonic solution when the grid was sufficiently refined. Second, we compared our results with those from the TOUGH2 [*Pruess*, 1991] code which uses a Newton-Raphson linearization with the choice of conjugate gradient solver (as opposed to our use of the MPI method along with the LR solver for the 2-D cases). The 2-D results using TOUGH2 were identical to those obtained with our solution approach.

4.2. Two-Phase Flow Simulations

Considering the diffusive nature of parabolic PDEs, coupling an additional such PDE should not change the fundamental behavior of the solution. In addition, for an open and isothermal system such as we consider here (i.e., when the air phase is allowed to escape and changes in the temperature within the system are negligible and thus do not influence fluid densities and viscosities), the air phase does not, in general, alter water imbibition. Thus the RE should contain all the relevant traditional physics. Nevertheless, to fully satisfy ourselves, we used the TOUGH2 [*Pruess*, 1991] code to conduct a series of two-phase (i.e., air-water) simulations, where air could escape out of the bottom of the problem domain, and compared the results to the cases where only the water phase was considered. High-resolution two-phase flow simulations revealed that when the air phase is included, the water saturation, similar to the single-phase cases, is monotonic and the plume is diffusive. Finally, we note that when *Ritsema et al*. [1998a] considered the full two-phase flow equations, as for the RE, they had to apply downwinding to the water phase to simulate fingers.

4.3. Changes in the Hydraulic Properties

While the parameter values for the hydraulic properties used in this study were representative of sands where fingers occur and properties have been measured, let us consider artificially changing them. We note that once we nondimensionalize the problem, the number of hydraulic property parameters reduce to only two (i.e., the size of the hysteresis loop α_H^*, and the media nonlinearity n_{PWC}). The first of these, α_H^*, becomes relevant only if a hysteretic reversal occurs and we have shown that the RE does not support the oversaturation that is required for such a reversal. The second, n_{PWC}, could be artificially increased such as to sharpen the front as might be presumed to occur under dynamic conditions. However, we found that as long as the grid spacing is chosen small enough, the solution will remain monotonic and thus the converged (i.e., grid-independent) solution will not yield a gravity-driven finger.

Regarding a reduction in the capillary pressure, the data of *Selker et al*. [1992] indeed suggests that the capillary pressure at finger tips is somewhat reduced from the presumed minimum of $\sim 1/\alpha_{\mathrm{PWC}}$; however, the water remains under tension for hydrophilic sands, and the reduction is on the order of a factor of $\sim$0.5. If we ignore possible dynamic influences on the Darcy-Buckingham flux law, the constitutive relations, or the equation of state that would change our problem from the RE with standard monotonic properties, our dimensionless approach can treat such a depression through the scaling with α_{PWC}. Since our solutions are all dimensionless, an increase in α_{PWC} of 2 will shrink the saturation field in Plate 1d to half its size, thus decreasing the plume length and width by about half (note that the source width must also be correspondingly decreased). However, this scaled field also corresponds to a field at half the time. Such changes influence both the horizontal and vertical scales identically, and so at much longer times and larger domains, while a plume may appear more slender and finger-like, it will not contain the nonmonotonic signature of a gravity-driven finger no matter how far α_{PWC} is increased. We also note that increasing α_{PWC} artificially reduces (or removes for dramatic increases in α_{PWC}) both capillary rise and horizontal imbibition, which in comparison to experiments, are both rapid and significant for hydrophilic sands where gravity-driven fingering occurs.

It is interesting to note that a reduction in the capillary pressure has been used recently to simulate preferential or fingered flow in heterogeneous unsaturated rock fractures with the RE [e.g., *Pruess*, 1998, 1999; *Pruess et al*., 1999]. The simulations presented in these papers indeed yield finger-like solutions that appear strikingly realistic. On closer examination, however, the fingers are found to actually follow high-permeability pathways and avoid lower-permeability grid blocks. In reality, capillary forces in low-permeability zones will significantly alter the flow structure by pulling water preferentially into them from high-permeability zones as can be demonstrated in the laboratory [e.g., see *Glass and Nicholl*, 1996, Figures 10 and 11].

Finally, we emphasize that if the values of the hydraulic parameters such as n_{PWC} and α_{PWC} are modified by dynamic conditions, these modifications must hold within the entire problem for all time and space in order for the properties to remain standard and monotonic. Because such modifications will not yield gravity-driven fingers, we are left to hypothesize nonstandard or nontraditional alternatives, each of which would incorporate additional physics. Such alternatives include but are not limited to a dynamic capillary pressure resulting in nonstandard equations of state; modified nonmonotonic constitutive relations for the relative permeability; and/or entirely different formulations of the flux law itself.

5. Concluding Remarks

As suggested by *Nieber* [1996], we confirmed that the RE with hysteresis and a downwind averaging method can simulate

finger-like behavior. However, we found that these fingers are numerical artifacts caused by a LTE term-induced oscillation that arises from the highly inaccurate nature of the downwind method. When we reduced the magnitude of the LTE terms through grid refinement, the finger-like nonmonotonic signature fades, and the WF eventually becomes monotonic. The more than 1 order of magnitude greater error of DW1 (relative to CD2) makes its LTE terms highly persistent, and to obtain an oscillation-free solution, DW1 requires extreme grid refinement. Moreover, downwind methods are inherently unstable [e.g., *Roache*, 1972, p. 68] and in the absence of a diffusive effect (i.e., the capillary term in the RE) do not yield bounded numerical solutions. Making use of an approach such as downwinding that relies on the LTE terms and subsequent numerical oscillation to simulate a physical phenomenon is problematic. Even while many aspects of the physical behavior can be mimicked through calibration of various numerical parameters, such an approach is not general and cannot be used to explore the true physical phenomenon within parameter space.

Thus we conclude that the RE along with standard monotonic constitutive relations and hysteretic equations of state cannot support a physically nonmonotonic flow response for a constant flux boundary condition. Since such physical nonmonotonicity is an essential characteristic of gravity-driven fingers, standard unsaturated flow theory (i.e., either the flux law and/or the standard monotonic properties) is insufficient to describe all aspects of unsaturated flow physics especially for infiltration in initially dry, highly nonlinear, and hysteretic media where gravity-driven fingers occur. We are certainly not the first to question the generality or even the validity of the RE [e.g., see *Gray and Hassanizadeh*, 1991; *Stonestrom and Akstin*, 1994]. However, in the context of gravity-driven fingering, the dramatically deviant physical behavior is a clear manifestation of the shortcomings of traditional theory.

Appendix A: Truncation Error for Various Terms of Richards Equation

Haverkamp and Vauclin [1979] presented temporal and spatial local truncation error (TE) terms of a number of averaging methods. Here we use the finite difference (FD) discretization of each RE component, and state the corresponding power series forms of the TE terms, for uniform grid spacing, as

Temporal derivative

$$\frac{(\Psi_{i,j}^{\nu+1} - \Psi_{i,j}^{\nu})}{\Delta\tau} = \frac{\partial\Psi}{\partial\tau} + \sum_{\nu=1}^{\infty}\left\{\left[\frac{\Delta\tau^{\nu}}{(\nu+1)!}\right]\left[\frac{\partial^{\nu+1}\Psi}{\partial\tau^{\nu+1}}\right]\right\}, \tag{A1}$$

Capillary component in the horizontal direction

$$\frac{1}{\Delta\eta^2}\left[\kappa_{i+1/2,j}^{\nu+1}(\Psi_{i+1,j}^{\nu+1} - \Psi_{i,j}^{\nu+1}) - \kappa_{i-1/2,j}^{\nu+1}(\Psi_{i,j}^{\nu+1} - \Psi_{i-1,j}^{\nu+1})\right] = \frac{\partial}{\partial\eta}\left[\kappa(\Psi)\frac{\partial\Psi}{\partial\eta}\right] + E_{\mathrm{cap}}(\eta), \tag{A2}$$

Capillary component in the vertical direction

$$\frac{1}{\Delta\xi^2}\left[\kappa_{i,j+1/2}^{\nu+1}(\Psi_{i,j+1}^{\nu+1} - \Psi_{i,j}^{\nu+1}) - \kappa_{i,j-1/2}^{\nu+1}(\Psi_{i,j}^{\nu+1} - \Psi_{i,j-1}^{\nu+1})\right] = \frac{\partial}{\partial\xi}\left[\kappa(\Psi)\frac{\partial\Psi}{\partial\xi}\right] + E_{\mathrm{cap}}(\xi), \tag{A3}$$

Gravity component

$$\frac{1}{\Delta\xi}\left[\kappa_{i,j+1/2}^{\nu+1} - \kappa_{i,j+1/2}^{\nu+1}\right] = \frac{\partial\kappa}{\partial\xi} + \sum_{j=1}^{\infty}\beta_j\left(\frac{\partial^{j+1}\kappa}{\partial\xi^{j+1}}\right). \tag{A4}$$

The first term on the RHS of each equation is the differential form, and the second term is the TE term. $E_{\mathrm{cap}}(\eta)$ and $E_{\mathrm{cap}}(\xi)$ are the error due to the capillary components in the η and ξ directions, respectively, and β_j is the spatial (i.e., grid spacing dependent) coefficient. β_j, $E_{\mathrm{cap}}(\eta)$, and $E_{\mathrm{cap}}(\xi)$ depend upon the averaging method. For the PDC method (i.e., DW1, CD2, and UW1), β_j has the following general form:

$$\beta_j = \frac{1}{2}\left[(1-w) + (1+w)(-1)^{j+1}\right]\left[\frac{\Delta\xi^j}{(j+1)!}\right] \qquad j = 1, 2, 3, \ldots, \tag{A5}$$

and for the CD3, β_j becomes

$$\beta_j = \frac{1}{3}\left[1 + (-1)^{j+1}(2^j - 3)\right]\left[\frac{\Delta\xi^j}{(j+1)!}\right] \qquad j = 3, 4, 5, \ldots, \tag{A6}$$

We can generally state the capillary component's LTE term in the ξ direction, $E_{\mathrm{cap}}(\xi)$, as

$$E_{\mathrm{cap}}(\xi) = we_0(\xi) + e_1(\xi) + 2\kappa e_2(\xi) + e_3(\xi), \tag{A7}$$

where

$$e_0(\xi) = \sum_{j=0}^{\infty}\left\{\frac{\Delta\xi^{2j+1}}{2(j+1)!}\right\}\left\{\frac{\partial\kappa}{\partial\xi}\frac{\partial^{2(j+1)}\Psi}{\partial\xi^{2(j+1)}} + \frac{\partial\Psi}{\partial\xi}\frac{\partial^{2(j+1)}\kappa}{\partial\xi^{2(j+1)}}\right\}, \tag{A8}$$

$$e_1(\xi) = \sum_{j=1}^{\infty}\left\{\frac{\Delta\xi^{2j}}{(2j+1)!}\right\}\left\{\frac{\partial\kappa}{\partial\xi}\frac{\partial^{2j+1}\Psi}{\partial\xi^{2j+1}} + \frac{\partial\Psi}{\partial\xi}\frac{\partial^{2j+1}\kappa}{\partial\xi^{2j+1}}\right\}, \tag{A9}$$

$$e_2(\xi) = \sum_{j=1}^{\infty}\left\{\frac{\Delta\xi^{2j}}{2(j+1)!}\right\}\left\{\frac{\partial^{2(j+1)}\Psi}{\partial\xi^{2(j+1)}}\right\}, \tag{A10}$$

$$e_3(\xi) = \sum_{j=2}^{\infty}\sum_{\ell=1}^{\infty}A_{\ell j}\left\{\frac{\Delta\xi^{j+\ell-1}}{j!(\ell+1)!}\right\}\left\{\frac{\partial^j\kappa}{\partial\xi^j}\frac{\partial^{\ell+1}\Psi}{\partial\xi^{\ell+1}}\right\}, \tag{A11}$$

and

$$A_{\ell j} = \frac{1+w}{2} + \frac{1-w}{2}(-1)^{j+\ell+1}. \tag{A12}$$

Note that a similar set of relations as (A7) through (A12) must be also stated for η direction for $E_{\mathrm{cap}}(\eta)$.

Acknowledgments. This research was supported by the U.S. Department of Energy's Basic Energy Sciences Geoscience Research Program under contract DE-AC04-94 AL85000 at Sandia National Laboratories. We thank the three anonymous reviewers for their constructive comments on the manuscript. We also wish to thank M. T. van Genuchten for objectively reviewing this manuscript and providing many helpful suggestions. Results demonstrating the artificial nature of "finger-like" solutions with the RE were first presented by *Eliassi and Glass* [1997].

References

Anderson, D. A., J. C. Tannehill, and R. H. Pletcher, *Computational Fluid Mechanics and Heat Transfer*, Taylor and Francis, Philadelphia, Pa., 1984.

Celia, M. A., E. T. Bouloutas, and R. L. Zarba, A general mass-conservative numerical solution for the unsaturated flow equation, *Water Resour. Res.*, *26*, 1483–1496, 1990.

Chouke, R. L., P. van Meurs, and C. van der Poel, The instability of slow immiscible, viscous, liquid-liquid displacements in porous media, *Trans. Am. Inst. Min. Eng.*, *216*, 188–194, 1959.

Cooley, R. L., Some new procedures for numerical solutions of variably saturated flow problems, *Water Resour. Res.*, *19*, 1271–1285, 1983.

Eliassi, M., and R. J. Glass, Implementation of implicit total variation diminishing methods for monotonic solution of Richards equation: The end of wiggles, false reversals, and numerical fingers (abstract), *Eos Trans. AGU*, *78*(46), Fall Meet. Suppl., 215–216, 1997.

Forsyth, P. A., and M. C. Kropinski, Monotonicity consideration for saturated-unsaturated subsurface flow, *SIAM J. Sci. Comput.*, *18*, 1328–1354, 1997.

Glass, R. J., and M. J. Nicholl, Physics of gravity driven fingering of immiscible fluids within porous media: An overview of current understanding and selected complicating factors, *Geoderma*, *70*, 133–163, 1996.

Glass, R. J., J.-Y. Parlange, and T. S. Steenhuis, Wetting front instability, 1, Theoretical discussion and dimensional analysis, *Water Resour. Res.*, *25*, 1187–1194, 1989a.

Glass, R. J., T. S. Steenhuis, and J.-Y. Parlange, Mechanism for finger persistence in homogenous unsaturated, porous media: Theory and verification, *Soil Sci.*, *148*, 60–70, 1989b.

Glass, R. J., T. S. Steenhuis, and J.-Y. Parlange, Wetting front instability, 2, Experimental determination of relationships between system parameters and two-dimensional unstable flow field behavior in initially dry porous media, *Water Resour. Res.*, *25*, 1195–1207, 1989c.

Gray, W. G., and S. M. Hassanizadeh, Paradoxes and realities in unsaturated flow theory, *Water Resour. Res.*, *27*, 1847–1854, 1991.

Gresho, P. M., and R. L. Lee, Don't suppress the wiggles—They're telling you something, *Comput. Fluids*, *9*, 223–253, 1981.

Harlow, F. H., and A. A. Amsden, Numerical calculation of multiphase fluid flow, *J. Comput. Phys.*, *17*, 19–52, 1975.

Haverkamp, R., and M. Vauclin, A note on estimating finite difference interblock hydraulic conductivity values for transient unsaturated flow problems, *Water Resour. Res.*, *15*, 181–187, 1979.

Hill, D. E., and J.-Y. Parlange, Wetting front instability in layered soils, *Soil Sci. Soc. Am. Proc.*, *36*, 697–702, 1972.

Hogarth, W. L., J. Hopmans, J.-Y. Parlange, and R. Haverkamp, Application of a simple soil water hysteresis model, *J. Hydrol.*, *98*, 21–29, 1988.

Kool, J. B., and J. C. Parker, Development and evaluation of closed-form expressions of hysteretic soil hydraulic properties, *Water Resour. Res.*, *23*, 105–114, 1987.

Kool, J. B., and M. T. van Genuchten, HYDRUS, One-dimensional variably saturated flow and transport model, including hysteresis and root water uptake, U.S. Salinity Lab., U.S. Dep. of Agric., Riverside, Calif., 1991.

Leonard, B. P., A survey of finite differences of opinion on numerical muddling of the incomprehensible defective confusion equation, in *Finite Element Methods in Convection Dominated Flows*, edited by T. J. R. Hughes, pp. 1–17, Am. Soc. of Mech. Eng., New York, 1979.

Leonard, B. P., and H. S. Niknafs, Sharp monotonic resolution of discontinuities without clipping of narrow extrema, *Comput. Fluids*, *19*, 141–154, 1991.

Liu, J., G. A. Pope, and K. Sepehrnoori, A high-resolution finite-difference scheme for nonuniform grids, *Appl. Math. Modell.*, *19*, 162–172, 1995.

Mualem, Y., A conceptual model of hysteresis, *Water Resour. Res.*, *10*, 514–520, 1974.

Mualem, Y., A new model for predicting the hydraulic conductivity of unsaturated porous media, *Water Resour. Res.*, *12*, 513–522, 1976.

Mualem, Y., A modified dependent-domain theory of hysteresis, *Soil Sci.*, *137*, 283–291, 1984.

Nguyen, H. V., J. L. Nieber, C. J. Ritsema, L. W. Dekker, and T. S. Steenhuis, Modeling gravity driven unstable flow in a water repellent soil, *J. Hydrol.*, *215*, 202–214, 1999a.

Nguyen, H. V., J. L. Nieber, P. Oduro, C. J. Ritsema, L. W. Dekker, and T. S. Steenhuis, Modeling solute transport in a water repellent soil, *J. Hydrol.*, *215*, 188–201, 1999b.

Nieber, J. L., Modeling finger development and persistence in initially dry porous media, *Geoderma*, *70*, 207–229, 1996.

Nieber, J. L., T. W. J. Bauters, T. S. Steenhuis, and J.-Y. Parlange, Numerical simulation of experimental gravity-driven unstable flow in water repellent sand, *J. Hydrol.*, *231–232*, 295–307, 2000.

Norton, D. L., Evaluation, extension, and application of a full field light transmission technique for the investigation of hysteresis in thin homogenous slabs, Ph.D. dissertation, Univ. of Ariz., Tucson, 1995.

Palmquist, W. N., and A. I. Johnson, Model study of infiltration into layered materials, paper presented at American Society of Civil Engineers Annual Meeting, Boston, Mass., Oct. 10–14, 1960.

Palmquist, W. N., and A. I. Johnson, Vadose zone in layered non layered materials, *Geol. Surv. Res.*, *119*, 142–143, 1962.

Patel, M. K., N. C. Markatos, and M. Cross, A critical evaluation of seven discretization schemes for convection-diffusion equations, *Int. J. Numer. Methods Fluids*, *5*, 225–244, 1985.

Peck, A. J., Moisture profile development and air compression during water uptake by bounded porous bodies: 3 vertical columns, *Soil Sci.*, *100*, 44–51, 1965.

Press, W. H., S. A. Teukolsky, W. T. Vetterling, and B. P. Flannery, *Numerical Recipes in C*, Cambridge Univ. Press, New York, 1992.

Pruess, K., TOUGH2—A general purpose numerical simulator for multiphase fluid and heat flow, *Rep. LBL-29400*, Lawrence Berkeley Natl. Lab., Berkeley, Calif., 1991.

Pruess, K., On water seepage and fast preferential flow in heterogeneous, unsaturated rock fractures, *J. Contam. Hydrol.*, *30*, 333–362, 1998.

Pruess, K., A mechanistic model for water seepage through thick unsaturated zones in fractured rocks of low matrix permeability, *Water Resour. Res.*, *35*, 1039–1051, 1999.

Pruess, K., B. Faybishenko, and G. S. Bodvarsson, Alternative concepts and approaches for modeling flow and transport in thick unsaturated zones of fractured rocks, *J. Contam. Hydrol.*, *38*, 281–322, 1999.

Ritsema, C. J., L. W. Dekker, J. L. Nieber, and T. S. Steenhuis, Modeling and field evidence of finger formation and finger recurrence in a water repellent sandy soil, *Water Resour. Res.*, *34*, 555–567, 1998a.

Ritsema, C. J., J. L. Nieber, L. W. Dekker, and T. S. Steenhuis, Stable or unstable wetting fronts in water repellent soils—Effect of antecedent soil moisture content, *Soil Tillage Res.*, *47*, 111–123, 1998b.

Roache, P. J., *Computational Fluid Dynamics*, Hermosa, Albuquerque, N. M., 1972.

Rubin, J., and R. Steinhardt, Soil water relations during rain infiltration, I, Theory, *Soil Sci. Soc. Am. Proc.*, *27*, 246–251, 1963.

Rubin, J., R. Steinhardt, and P. Reiniger, Soil water relations during rain infiltration, II, Moisture content profiles during rains of low intensities, *Soil Sci. Soc. Am. Proc.*, *28*, 1–5, 1964.

Saffman, P. G., and G. I. Taylor, The penetration of a fluid into a porous medium or Hele-Shaw cell containing a more viscous liquid, *Proc. R. Soc. London*, *Ser. A*, *245*, 312–331, 1958.

Scott, P. S., G. J. Farquhar, and N. Kouwen, Hysteretic effects on net infiltration, in *Advances in Infiltration*, *Publ. 11-83*, pp. 163–170, Am. Soc. Agric. Eng., St. Joseph, Mich., 1983.

Selker, J. S., P. Leclerq, J.-Y. Parlange, and T. S. Steenhuis, Fingered flow in two dimension, 1, Measurements of matric potential, *Water Resour. Res.*, *28*, 2513–2521, 1992.

Stonestrom, D. A., and K. C. Akstin, Nonmonotonic matric pressure histories during constant flux infiltration into homogenous profiles, *Water Resour. Res.*, *30*, 81–91, 1994.

Tabuchi, T., Infiltration and ensuing percolation in columns of layered glass particles packed in laboratory, *Nogyo Dobuku Kenkyn Bessatsu* (*Trans. Agric. Eng. Soc. Jpn.*), *1*, 13–19, 1961.

Talsma, T., Hysteresis in two sands and the independent domain model, *Water Resour. Res.*, *6*, 964–970, 1970.

Topp, G. C., and E. E. Miller, Hysteretic moisture characteristics and hydraulic conductivities for glass-bead media, *Soil Sci. Soc. Am. Proc.*, *30*, 156–162, 1966.

Vachaud, G., and J.-L. Thony, Hysteresis during infiltration and redistribution in a soil column at different initial water contents, *Water Resour. Res.*, *7*, 111–127, 1971.

van Genuchten, M. T., A closed-form equation for predicting the hydraulic properties of unsaturated soils, *Soil Sci. Soc. Am. J.*, *44*, 892–898, 1980.

Warming, R. F., and B. J. Hyett, The modified equation approach to the stability and accuracy analysis of finite-difference methods, *J. Comput. Phys.*, *14*, 159–179, 1974.

Youngs, E. G., Developments in physics of infiltration, *Soil Sci. Soc. Am. J.*, *59*, 307–313, 1995.

Zaidel, J., and D. Russo, Estimation of finite difference interblock conductivities for simulation of infiltration into initially dry soils, *Water Resour. Res.*, *28*, 2285–2295, 1992.

M. Eliassi and R. J. Glass, Flow Visualization and Processes Laboratory, Sandia National Laboratories, Albuquerque, NM 87185-0735. (meliass@sandia.gov; rjglass@sandia.gov)

(Received September 26, 2000; revised December 12, 2000; accepted December 13, 2000.)